SANDIA REPORT

SAND90—0253 • UC—814
Unlimited Release
Printed July 1991

Yucca Mountain Site Characterization Project

A Boundary Integral Equation Method for Steady Two-Dimensional Flow in Partially Saturated Media

M. J. Martinez, D. F. McTigue

Prepared by
Sandia National Laboratories
Albuquerque, New Mexico 87185 and Livermore, California 94550
for the United States Department of Energy
under Contract DE-AC04-76DP00789

"Prepared by Yucca Mountain Site Characterization Project (YMSCP) participants as part of the Civilian Radioactive Waste Management Program (CRWM). The YMSCP is managed by the Yucca Mountain Project Office of the U.S. Department of Energy, Nevada Operations Office (DOE/NV). YMSCP work is sponsored by the Office of Geologic Repositories (OGR) of the DOE Office of Civilian Radioactive Waste Management (OCRWM)."

Issued by Sandia National Laboratories, operated for the United States Department of Energy by Sandia Corporation.

Available to DOE and DOE contractors from
Office of Scientific and Technical Information
PO Box 62
Oak Ridge, TN 37831

Prices available from (615) 576-8401, FTS 626-8401

Available to the public from
National Technical Information Service
US Department of Commerce
5285 Port Royal Rd
Springfield, VA 22161

NTIS price codes
Printed copy: A04
Microfiche copy: A01

SAND90-0253
Unlimited Release
Printed July 1991

SAND--90-0253

DE91 016056

A Boundary Integral Equation Method for Steady Two-Dimensional Flow in Partially Saturated Media

M. J. Martinez
D. F. McTigue

Fluid Mechanics and Heat Transfer Division
Sandia National Laboratories
Albuquerque, New Mexico 87185

Abstract

The governing equation for steady flow in a partially saturated, porous medium can be written in a linear form if one adopts a hydraulic conductivity function that is exponential in the capillary-pressure head. The resulting linear field equation is well suited to numerical solution by the boundary integral equation method (BIEM). The exponential conductivity function is compared to a more complex form often assumed for tuffs, and is found to be a reasonable approximation over limited ranges of pressure head. A computer code based on the BIEM is described and tested. The BIEM is found to exhibit quadratic convergence with element size reduction on smooth solutions and on singular problems, if mesh grading is used. Agreement between results from the BIEM code and a finite-element code that solves the fully nonlinear problem is excellent, and is achieved at a substantial advantage in computer processing time.

The work contained in this report was done at Quality Assurance Level NQ and pertains to WBS Element 1.2.1.4.4.1.

Contents

Figures

Tables

1 Introduction

It is apparent that many, large simulations may be required to investigate the effects of material heterogeneity on the hydrology of Yucca Mountain. The governing equations for flow in partially saturated media are, in general, highly nonlinear, and solutions embracing the full complexity of some current models may be prohibitively slow and costly. Thus, it is important to explore any approximations and/or new solution methods that offer the potential for greatly improved speed, while retaining the critical elements of the transport phenomena.

This report presents one such approach. Here, we consider steady, multidimensional flows, and adopt the exponential form for the hydraulic conductivity. It is recognized that other, more complex forms for the conductivity yield better fits to data for some materials, particularly when considering a broad range of capillary pressure head. However, we argue that, for certain classes of problems, the more complex forms offer no significant advantage over the exponential form, while the latter offers potentially large gains in ease of solution.

For the exponential conductivity model, a simple change of dependent variable renders the governing equation linear. This process is referred to as the "quasi-linear transformation" following Philip (1968). The enormous simplification effected by the transformation apparently was first noted by Gardner (1958), and has been exploited since by numerous workers, most notably Philip. Comprehensive reviews of the approach and its application have been presented by Philip (1969, 1989) and Pullan (1990). The linear governing equation, of course, admits of much simpler and faster solution methods than does the original, nonlinear equation. In this report, we explore the boundary integral equation method (BIEM) for obtaining numerical solutions in arbitrary two-dimensional geometries. This scheme, apparently first applied in this context by Pullan and Collins (1987), offers a number of significant advantages over other, more conventional approaches.

- The BIEM reduces the dimension of the numerical problem by one in comparison to more conventional domain methods (*e.g.*, finite difference or finite element), typically yielding a much smaller computational problem.
- The required data for computational purposes is significantly reduced for the BIEM because only the domain boundaries need be described, as opposed to requiring mesh data for the entire domain when using finite-difference or finite-element methods; furthermore, complicated geometry is easily accommodated because only the boundaries need be specified.
- The BIEM treats problems in unbounded domains naturally because the fundamental solutions employed satisfy far-field boundary conditions identically.
- The BIEM yields fluxes that retain accuracy of the same order as the potential itself because a numerical approximation for the gradient is not required.

Some of the limitations of the present approach are as follows:

- The exponential form for the conductivity may not give a good representation of data for a particular material over the pressure head range of interest.
- The transformed governing equation is valid only for heads less than or equal to zero; *i.e.*, the system of interest must remain unsaturated.
- The computation of potential and flux at numerous internal points may be time-consuming compared to computing the boundary values, although it remains a post-processing task; an interpolation scheme may be expedient if numerous internal points are required.
- The present formulation of the BIEM considers only homogeneous material; the treatment of interfaces between materials of contrasting properties requires further development.

Section 2 reviews the equations describing steady, unsaturated flow in porous material and its transformation to a linear governing equation. The applicability to tuff is addressed in Section 3 by comparisons of the exponential conductivity function to a more widely used, but more complex, representation. In Section 4, insight into the behavior of the model is provided through exact solutions for one-dimensional, vertical flow. An outline of the boundary integral equation method and the numerical treatment is given in Section 5, and further aspects of the numerical analysis are developed in Section 6. Section 7 presents some test problems in which the BIEM solutions are compared to independent results for two-dimensional domains. Finally, a summary is given in Section 8.

2 The Quasi-Linear Transformation

Mass conservation for steady flow in a rigid, porous medium is given simply by

$$\nabla \cdot \mathbf{q} = 0 \quad , \tag{2.1}$$

where $\mathbf{q}$ is the fluid flux (volume flow rate per unit area of the medium). The flux is assumed to be related to the pressure gradient and the gravitational body force by Darcy's law:

$$\mathbf{q} = -K(\psi)(\nabla\psi - \mathbf{e}_z) \quad , \tag{2.2}$$

where K is the hydraulic conductivity (here taken to be isotropic), ψ is the capillary pressure head, and $\mathbf{e}_z$ is the unit vector in the vertical direction (positive downward). The combination of (2.1) and (2.2) is the steady form of the Richards equation:

$$\nabla \cdot [K(\psi)(\nabla\psi - \mathbf{e}_z)] = 0 \quad . \tag{2.3}$$

Because the hydraulic conductivity K is a strongly varying function of ψ, this equation is, in general, highly nonlinear. It is instructive in the present context to rearrange (2.3) in the form

$$\nabla^2\psi + \frac{1}{K}\frac{dK}{d\psi}\left[\nabla\psi\cdot\nabla\psi - \frac{\partial\psi}{\partial z}\right] = 0 \quad , \tag{2.4}$$

showing that the slope of the conductivity function, $dK/d\psi$, as well as $K(\psi)$ itself, enters into the flow equation. This form of the flow equation assumes that $K(\psi)$ is unique, *i.e.*, hysteresis is not considered in this work.

2.1 Hydraulic Conductivity Models

An early model for the dependence of hydraulic conductivity upon pressure head was posed by Brooks and Corey (1966):

$$K(\psi) = K_s\left(\frac{|\psi|}{|\psi_b|}\right)^{-n} \quad , \quad |\psi| \geq |\psi_b| \quad , \tag{2.5}$$

where K_s is the saturated conductivity, ψ_b is the "bubbling" or "air-entry" head, and n is a material parameter.[1] Note that, in this model, $K \to K_s$ as $\psi \to \psi_b$, rather than as $\psi \to 0$.

A model in wide use currently is that posed by van Genuchten (1980):

$$K(\psi) = K_s\left(1 + |\alpha_v\psi|^\beta\right)^{-(\beta-1)/2\beta}\left[1 - \left(\frac{|\alpha_v\psi|^\beta}{1+|\alpha_v\psi|^\beta}\right)^{(\beta-1)/\beta}\right]^2 \quad , \tag{2.6}$$

where α_v and β ($\beta > 1$) are material constants. The van Genuchten model differs from the Brooks-Corey model in its asymptotic behavior for "wet" (small $|\psi|$) conditions, in that $K \to K_s$ as $\psi \to 0$, as one might expect. In fact,

$$K(\psi) = K_s\left[1 - 2|\alpha_v\psi|^{\beta-1} - \frac{(\beta-1)}{2\beta}|\alpha_v\psi|^\beta + O(|\alpha_v\psi|^{2\beta-1})\right] \quad , \tag{2.7}$$

as $\psi \to 0$. Note, however, that the slope of $K(\psi)$ (*cf.* equation 2.4) is unbounded near saturation if $\beta < 2$, i.e.,

$$\frac{1}{K_s}\frac{dK}{d\psi} = 2\alpha_v(\beta-1)|\alpha_v\psi|^{\beta-2} + \frac{1}{2}\alpha_v(\beta-1)|\alpha_v\psi|^{\beta-1} + O(|\alpha_v\psi|^{2\beta-2}) \quad . \tag{2.8}$$

This feature of the van Genuchten model, for $\beta < 2$, can be troublesome in obtaining numerical solutions near saturated regions, although an empirical solution is simply to avoid the singular point (*e.g.*, saturated boundaries can be specified as $\psi = -\epsilon$, where ϵ is a suitably small number).

[1] The exponent n is related to the parameters λ and ϵ originally introduced by Brooks and Corey (1966) by $n = \lambda\epsilon = 2 + 3\lambda$.

In the "dry" limit (large $|\psi|$), the Brooks and Corey and van Genuchten models are of identical form; from (2.6):

$$\lim_{|\psi|\to\infty} K(\psi) = K_s \left(\frac{\beta-1}{\beta}\right)^2 |\alpha_v \psi|^{-(5\beta-1)/2} \quad . \tag{2.9}$$

The equivalent to the Brooks-Corey exponent (2.5) is then given by $n \equiv (5\beta-1)/2$, and the equivalent to the bubbling head is given by

$$|\psi_b| \equiv \left(\frac{\beta-1}{\beta}\right)^{4/(5\beta-1)} \alpha_v^{-1} \quad . \tag{2.10}$$

Equation (2.10) shows that the bubbling head approaches α_v^{-1} for large values of β, and vanishes as β approaches unity. Thus, large values of β correspond to conductivity curves exhibiting a "shoulder" where the conductivity begins to drop off rapidly with increasing $|\psi|$.

A simpler form for $K(\psi)$ that is often used in soil physics is the exponential form:

$$K(\psi) = K_s \exp(-\alpha|\psi|) \quad , \tag{2.11}$$

where α is a material constant. Clearly, $-\alpha$ is simply the slope of a plot of $\ln K$ *vs.* $|\psi|$.

It is obvious that (2.6) is capable of representing a more complex trend than either of (2.5) or (2.11), if only because (2.6) is a three-parameter model, while (2.11) is a two-parameter model. The Brooks and Corey model, (2.5), is stricly speaking a three-parameter model, however it is very similar to the exponential model. The two are in fact of identical form in the dry limit, as noted above. They are also similar in the wet limit, when the exponential is written as in (2.12), to be discussed shortly. Nonetheless, it can be shown that (2.11) yields a reasonable approximation to (2.6) for relatively small values of $|\psi|$, particularly when β is not large. It is worth noting here that, given this similarity over a limited range of pressure head, (2.11) is just as well-motivated as (2.6) within that range. This is particularly so in the many cases in which the choice of (2.6) is not based on its success in matching data. Rather, in these cases, the corollary to (2.6) for the pressure–saturation relationship is successful in matching data (*e.g.*, Klavetter and Peters, 1986), and the extension to a functional form for $K(\psi)$ is based on a model advanced originally by Mualem (1976). In the absence of conductivity data, there is no reason to prefer one model over the other within a range of $|\psi|$ in which the functions are of similar shape.

Often, too, one can argue that scenarios involving very low saturations, and correspondingly large capillary pressures, are unlikely. Thus, an accurate representation of the conductivity for very dry materials may not be critical. In any case, when $|\psi|$ is very large, the conductivity tends to zero, so essentially no flow occurs in those regions. Very large errors in the estimates of K in very dry regions can often be tolerated, because these regions do not participate in the flow.

At higher saturations, some materials exhibit a "shoulder" in the $K(\psi)$ curve; that is, K remains close to K_s until $|\psi|$ reaches some finite value, as indicated in the Brooks and Corey model (2.5), then falls off rapidly with increasing $|\psi|$. This is easily accommodated in the exponential model by modifying (2.11) to the form

$$K(\psi) = K_s(\psi_0) \exp\left[-\alpha(|\psi| - |\psi_0|)\right] \quad , \quad |\psi| \geq |\psi_0| \quad , \tag{2.12}$$

where ψ_0 is analogous to the bubbling, or air-entry, head. A "shoulder" in the $K(\psi)$ function can thus be approximated simply by adopting an "effective" saturated conductivity, $K_s \exp(\alpha|\psi_0|)$. Of course, one must then ensure that the magnitude of the pressure head does not exceed $|\psi_0|$ anywhere in the field of interest. In particular, when $\psi_1 \leq \psi \leq \psi_0$ Philip (1985) recommends the following prescription for determining α when $K(\psi)$ is known:

$$\alpha = \frac{K(\psi_0) - K(\psi_1)}{\int_{\psi_1}^{\psi_0} K(\psi) d\psi} \quad . \tag{2.13}$$

Philip finds that this recommendation is an optimal prescription for some particular geometries. This method of defining α, in combination with (2.12), is recommended for problems where the range of pressure head (or equivalently saturation) is known. On problems where the pressure range is not known *a priori*, the method could be used to improve a solution obtained with an initial estimate for α. The computed solution can be scanned to determine the pressure range, an improved α can be determined as described above, and a new, and presumedly improved, solution can be computed. This scheme is viable if an efficient numerical technique is available for solving (2.3), when the hydraulic conductivity is defined by (2.11) or (2.12), as we describe in the following sections.

2.2 The Linear Potential Problem

Combination of (2.3) and any of (2.5), (2.6), (2.11), or (2.12) yields a nonlinear equation for ψ, as is evident from inspection of (2.4). However, consider the introduction of a function Φ through the Kirchhoff transformation:

$$\Phi = \int_{\psi_0}^{\psi} K(\zeta) d\zeta \quad , \tag{2.14}$$

where ψ_0 is a constant. Differentiation of (2.14) and substitution into (2.3) yields

$$\nabla^2 \Phi - \left(\frac{1}{K}\frac{dK}{d\psi}\right)\frac{\partial \Phi}{\partial z} = 0 \quad . \tag{2.15}$$

In general, the Kirchoff transformation renders the flow equation in a quasi-linear form, and in the special case when $K^{-1}dK/d\psi$ is constant, equation (2.15) is clearly linear. The exponential conductivity functions given by (2.11) or (2.12) satisfy this condition.

In the present context, it is convenient to introduce a special case of the Kirchhoff transformation,

$$\phi = \exp(\alpha\psi) \quad , \tag{2.16}$$

which corresponds to (2.11), and is derived from (2.14) by making the identities $\psi_0 \to -\infty$ and $\phi = (\alpha/K_s)\Phi$. Substitution of (2.16) directly into (2.3) and (2.11) yields

$$\nabla^2\phi - \alpha\frac{\partial\phi}{\partial z} = 0 \quad , \tag{2.17}$$

which is a *linear* equation in ϕ. Comparison of (2.16) with (2.11) shows that equation (2.17) may be viewed alternatively as a governing equation for the relative conductivity field, K/K_s. Clearly, (2.17) is much easier to solve than equation (2.4) along with (2.11), (2.5), (2.6), or (2.12). Equation (2.17) has in fact been studied exhaustively (see Carslaw and Jeager, 1978) because it is identical in form to the equation governing steady convection and diffusion of a quantity ϕ, with $\alpha = w/\mathcal{D}$, where w is the (uniform) velocity in the $+z$ direction, and $\mathcal{D}$ is the diffusivity. Indeed, it is convenient that fundamental solutions to (2.17) are known in two and three dimensions (Section 5.3).

The usual boundary conditions are also linear. A specified head simply becomes a specified value of ϕ (*e.g.*, $\psi = 0$ corresponds to $\phi = 1$). A specified flux is also a linear condition; for example, for a constant vertical flux specified at some elevation z_0,

$$q_z(z_0) = q_0 \quad , \tag{2.18}$$

where q_0 is a positive constant, (2.2) and (2.11) give

$$\frac{\partial\phi}{\partial z}(z_0) - \alpha\phi(z_0) = -\frac{\alpha q_0}{K_s} \quad . \tag{2.19}$$

In the general case, the flux vector is a linear function of the potential,

$$\frac{\alpha\mathbf{q}}{K_s} = -\nabla\phi + \alpha\phi\mathbf{e}_z \quad . \tag{2.20}$$

However, it is important to note that one penalty paid for the change of variable is that the new potential ϕ is, in general, discontinuous at interfaces between contrasting materials. Consider a point $\mathbf{x}_b$ on a material interface. At this point, the pressure head must be continuous:

$$\psi_1(\mathbf{x}_b) = \psi_2(\mathbf{x}_b) \quad , \tag{2.21}$$

where ψ_1 and ψ_2 are the heads in materials 1 and 2, respectively. The matching condition in terms of ϕ then becomes, from (2.16):

$$\phi_1^{1/\alpha_1} = \phi_2^{1/\alpha_2} \quad \text{at} \quad \mathbf{x}_b \quad , \tag{2.22}$$

which is clearly nonlinear, as long as the materials have contrasting properties, $\alpha_1 \neq \alpha_2$.

3 Applicability

3.1 General Considerations

As discussed in Section 2.1, the exponential model for the unsaturated conductivity (2.11) is somewhat restrictive. It cannot describe the behavior of many materials, particularly when a broad range of capillary pressures is encountered. Some materials remain close to full saturation, with K remaining close to K_s, until $|\psi|$ reaches some finite value, above which the saturation and permeability drop off rapidly. In such cases, the exponential model can be modified slightly to account for the offset, (2.12). In the very dry range (large $|\psi|$), the exponential model also may fail to represent conductivity data. For many problems in unsaturated-zone hydrology, however, the conductivity at very low saturation is so small that no significant flow takes place, and an accurate representation of the function $K(\psi)$ is not critical.

There are several methods to determine α if the material permeability is known. In the following, we discuss and compare two techniques that appear promising. The first method is perhaps the more general, and is based upon the fact that $-\alpha$ is the slope of a plot of $\ln K$ *vs.* ψ. Hence, a "best value," in a least-squares sense, can be determined numerically by minimizing an appropriately defined error between the known data and a parametric representation. Here, the data from which α is determined can be respresented as $\ln K$ *vs.* ψ, or, in terms of the general definition of α, as $K^{-1}dK/d\psi$ *vs.* ψ. This latter definition arises upon application of the Kirchhoff transformation to the steady Richards equation (2.3). Another method, suggested by Philip (1985), is to define α according to (2.13).

3.2 Yucca Mountain Tuffs

It is emphasized again that hydraulic conductivity data for Yucca Mountain rocks are not available at this time. Saturated conductivities (K_s) have been measured, and the functional form of K/K_s is assumed to be fully determined by measurements of the pressure–saturation relationship following Mualem (1976) and van Genuchten (1980). As a starting point in estimating appropriate values for the parameter α in (2.11) for Yucca Mountain tuffs, and as a basis for direct comparisons between the van Genuchten and exponential models, the following procedure was carried out. For the sake of argument, the van Genuchten model (2.6) is accepted as "exact," and typical parameters obtained previously for tuff, as specified for the COVE 2A benchmarking exercise (*e.g.*, Hopkins, 1990), are adopted (Table 3.1). Steady-state, one-dimensional solutions have been obtained numerically for a number of different input fluxes (Hopkins, 1990), using the van Genuchten model (2.6). These simulations show that, for input fluxes of 0.1 mm/yr and above, the capillary pressure heads are never less than about -150 m. Thus, we restrict our attention to the range $0 \leq |\psi| \leq 150$ m. We use the van Genuchten form (2.6), with the parameters given in Table 3.1 to create "data" for $K(\psi)$ in this range. Then, retaining the specified value for K_s, we fit the exponential function (2.11) to these

Table 3.1. van Genuchten model parameters.

Unit	Saturated Conductivity (m/s)	α_v (m^{-1})	β
TC	9.7×10^{-12}	0.821×10^{-2}	1.558
PT	3.9×10^{-7}	1.500×10^{-2}	6.872
TS	1.9×10^{-11}	0.567×10^{-2}	1.798
CHnv	2.7×10^{-7}	1.600×10^{-2}	3.872
CHnz	2.0×10^{-11}	0.308×10^{-2}	1.602

Table 3.2. Exponential model parameters.

Unit	Saturated Conductivity (m/s)	α (m^{-1})
TC	9.7×10^{-12}	3.820×10^{-2}
PT	3.9×10^{-7}	1.713×10^{-2}
TS	1.9×10^{-11}	1.742×10^{-2}
CHnv	2.7×10^{-7}	2.219×10^{-2}
CHnz	2.0×10^{-11}	1.406×10^{-2}

"data" in order to determine α. The fits are performed with the parameter-estimation code ESTIM (Hills, 1987), and are based on minimizing the sum of squares of residuals, $K_{\text{exponential}} - K_{\text{vanGenuchten}}$.

Results are given in Table 3.2, and comparisons of the van Genuchten "data" and the exponential fit are shown in Figures 3.1–3.5. The fits are quite good for the Topopah Spring and Calico Hills zeolitic units, somewhat poorer for the Tiva Canyon, especially at higher values of $|\psi|$, and appear to be quite unsatisfactory for the Paintbrush and Calico Hills vitric tuffs. The latter is a consequence of the "shoulder" in the curves, represented in the van Genuchten model by relatively large values of β. This feature cannot be represented with the unmodified exponential form (2.11). Although the modified form (2.12) could be applied as a partial remedy, we do not do so here. Both linear-linear and semi-log plots are shown in order to illustrate the weight that tends to be given to the higher values of K using this scheme.

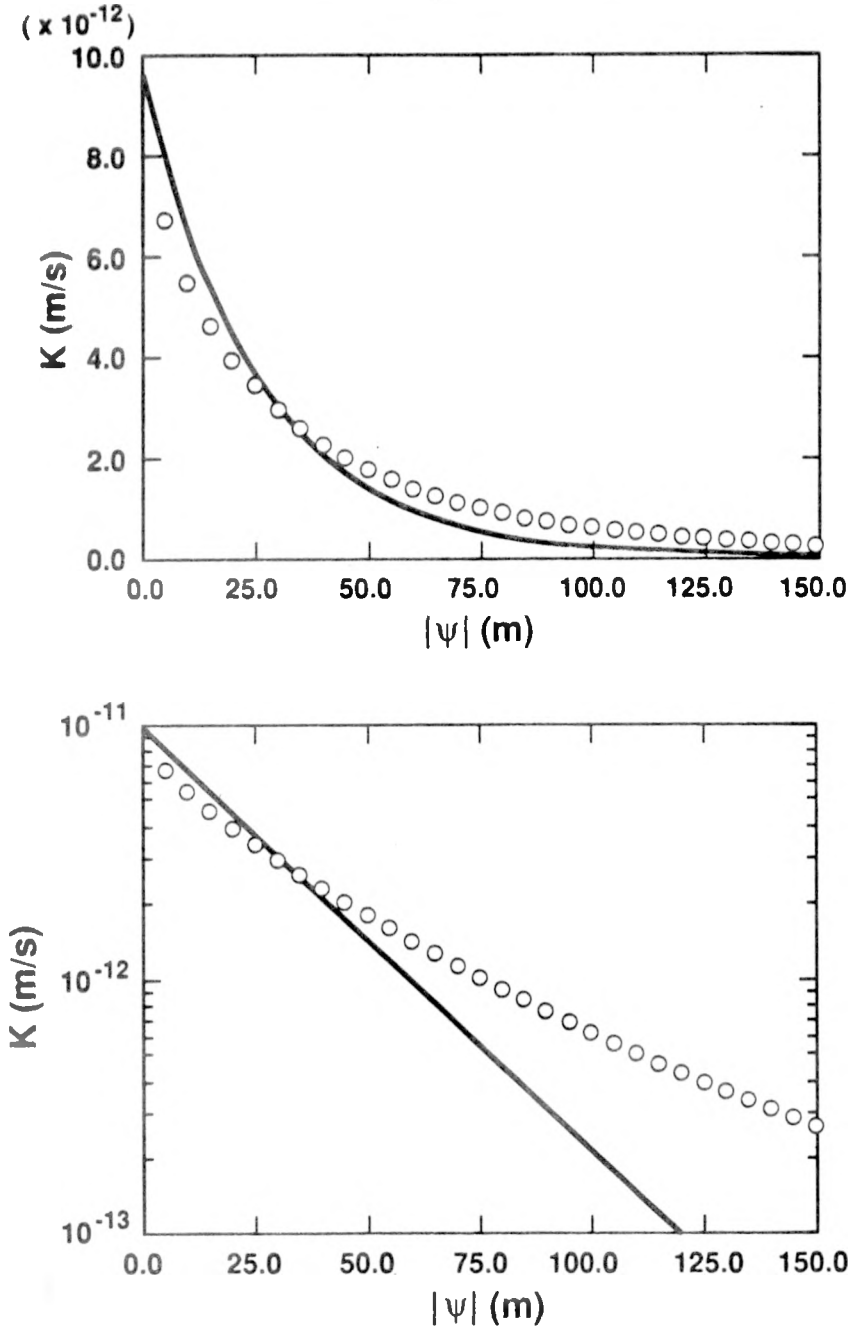

Figure 3.1. Comparison between the exponential (curves) and van Genuchten (symbols) representations for the hydraulic conductivity of the Tiva Canyon unit in (a) linear and (b) logarithmic coordinates.

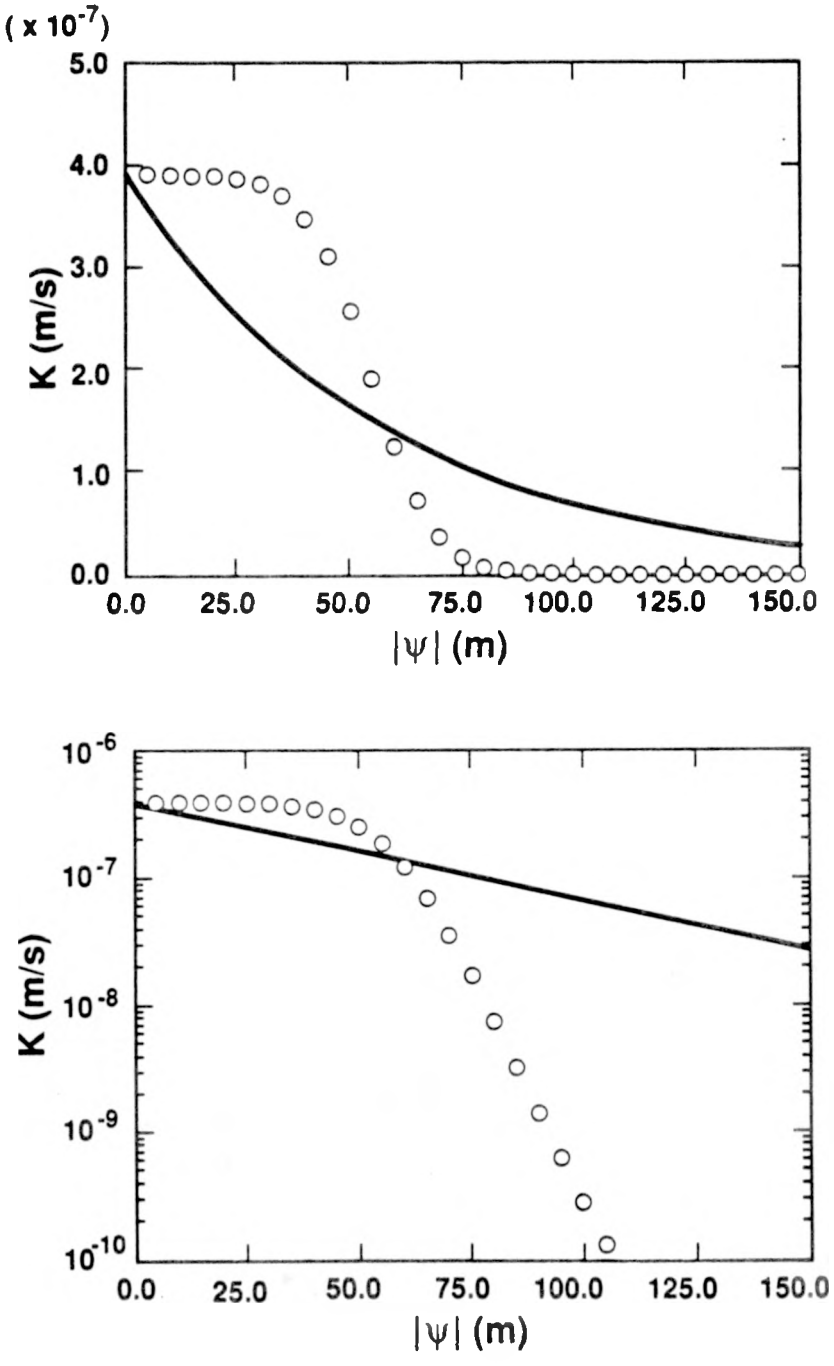

Figure 3.2. Comparison between the exponential (curves) and van Genuchten (symbols) representations for the hydraulic conductivity of the Paintbrush unit in (a) linear and (b) logarithmic coordinates.

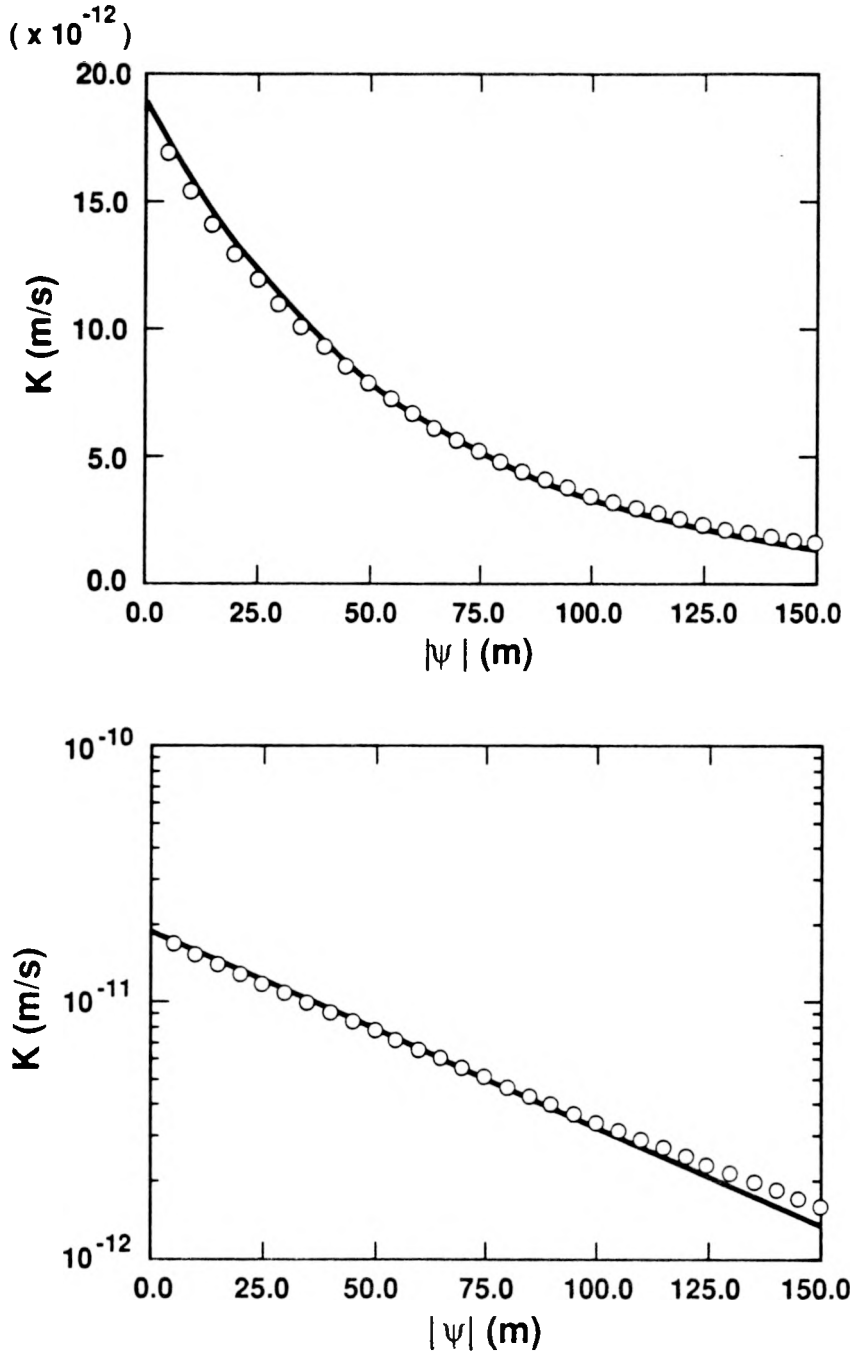

Figure 3.3. Comparison between the exponential (curves) and van Genuchten (symbols) representations for the hydraulic conductivity of the Topopah Spring unit in (a) linear and (b) logarithmic coordinates.

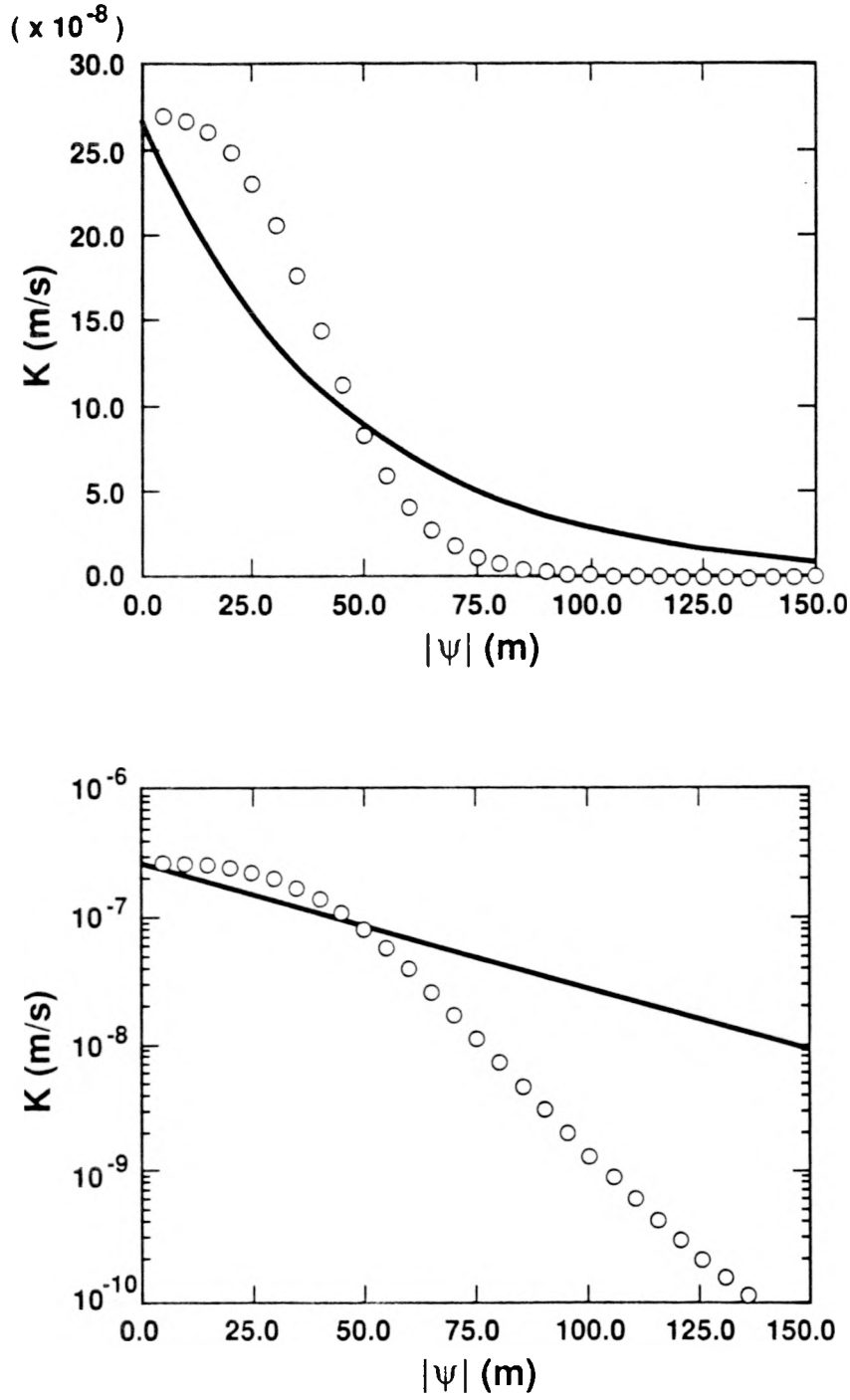

Figure 3.4. Comparison between the exponential (curves) and van Genuchten (symbols) representations for the hydraulic conductivity of the Calico Hills vitric unit in (a) linear and (b) logarithmic coordinates.

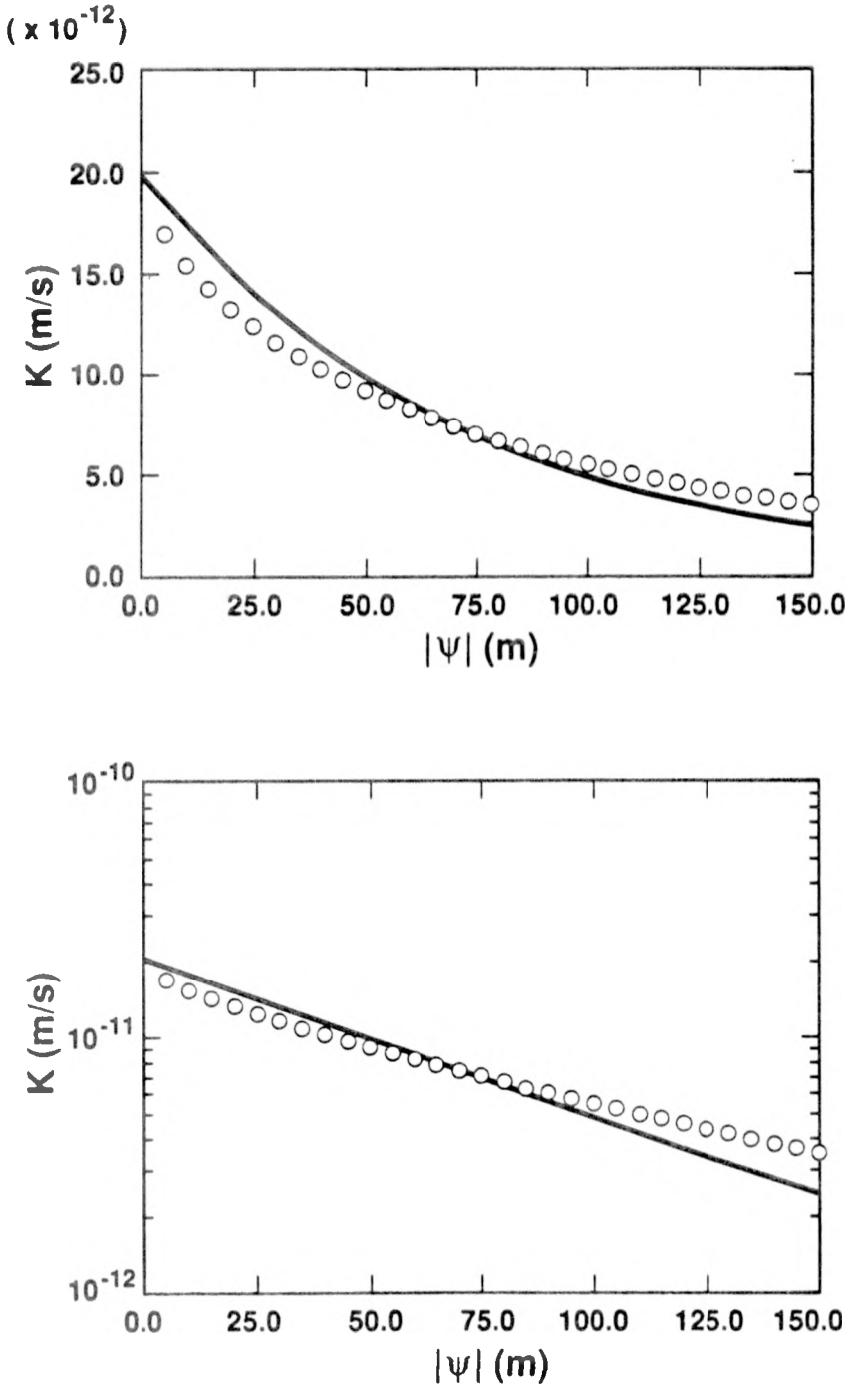

Figure 3.5. Comparison between the exponential (curves) and van Genuchten (symbols) representations for the hydraulic conductivity of the Calico Hills zeolitic unit in (a) linear and (b) logarithmic coordinates.

The second method of determining α utilizes Philip's prescription, defined in (2.13). This method also depends on a selection of a pressure head range, $\psi_1 \leq \psi \leq \psi_0$. The known functional form for hydraulic conductivity is again approximated by the van Genuchten function, with parameters as given in Table (3.1). Because we investigate the effect of the range of pressure head considered, we compute values of α for only two strata, the Topopah Spring and Calico Hills vitric units. In the preceding method, the former stratum was well represented by an exponential while the latter was not, for the pressure head range -150 m $\leq \psi \leq 0$. Figure 3.6 shows the variation of α as a function of ψ_1, the lower bound pressure head, for various values of the maximum pressure head, ψ_0. For the Topopah Spring unit, the variation of α with ψ_0 is modest for all values of ψ_0, with the exception of the case with $\psi_0 = 0$. The large variation of α when ψ_1 is near saturation ($\psi_0 = 0$) on this curve reflects the divergent behavior of the van Genuchten function when $\beta < 2$, as discussed earlier (Eqn. 2.8). Otherwise, the α computed by this method is only modestly dependent on the pressure range, which agrees with the "least-squares" method of determining α as discussed above. The variation of α for the Calico Hills vitric unit is also independent of the pressure head range if $\psi_1 < -75$ m. This is because the largest variation of K with ψ occurs for the pressure head range -75 m $< \psi < -40$ m (Figure 3.4). Hence, for given ψ_0, the variation of α occurs for $\psi_0 > \psi_1 > -75$ m. The values of α computed with this method agree well with those using the first method dicussed above. These correspond to $\psi_0 = 0$ and $\psi_1 = -150$ m, for which the figures show $\alpha = 0.0172$ m^{-1} and 0.0233 m^{-1}, for the Topopah Spring and Calico Hills vitric units, respectively. These compare favorably with the corresponding values from the "least-squares" method, viz., 0.0174 m^{-1} and 0.0222 m^{-1}, respectively.

4 One-Dimensional Flow

4.1 Exact Solution for a Single Layer

A useful test problem for which an analytical solution is easily obtained is that for steady, vertical flow. Clearly, from (2.1), the flux is everywhere constant, say $q_z(z) = q_\infty$. Then one integration of (2.17) yields

$$\frac{d\phi}{dz} - \alpha\phi = -\frac{\alpha q_\infty}{K_s} \quad . \tag{4.1}$$

For a specified potential at some level z_1, $\phi(z_1) = \phi_1$, another integration yields

$$\phi = \frac{q_\infty}{K_s} + \left(\phi_1 - \frac{q_\infty}{K_s}\right) \exp[\alpha(z - z_1)] \quad , \quad z < z_1 \quad . \tag{4.2}$$

This solution, for $z - z_1 \to -\infty$, goes asymptotically to the "unit-head-gradient" solution,

$$\lim_{z - z_1 \to -\infty} \phi = \frac{q_\infty}{K_s} \quad , \tag{4.3}$$

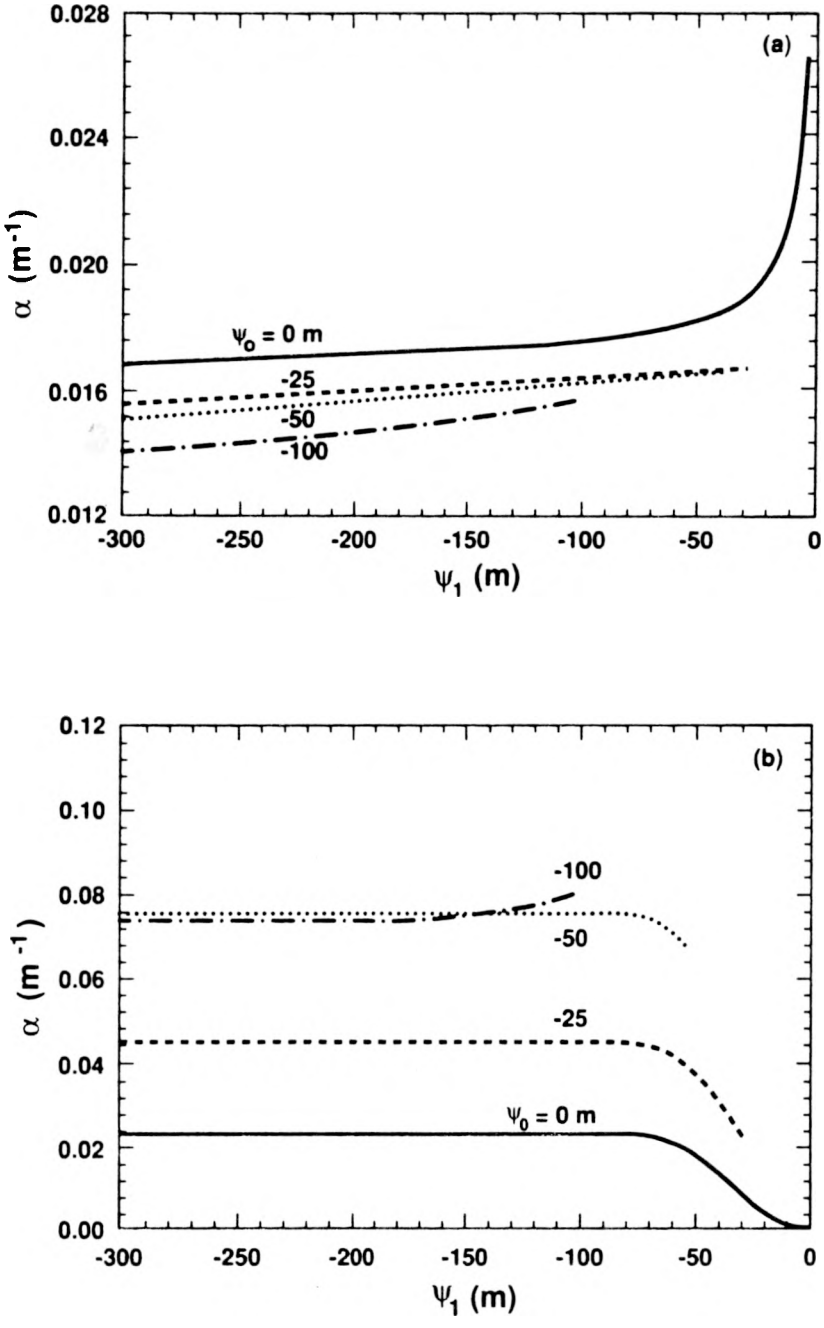

Figure 3.6. Philip's prescription for determining α as a function of the range of pressure head for the (a) Topopah Spring unit, and the (b) Calico Hills vitric unit. Each curve represents a different upper bound on pressure head ψ_0, while the lower bound pressure head, ψ_1 is varied with a small increment in pressure head.

or $\psi \rightarrow \alpha^{-1} \ln(q_\infty/K_s)$, where $0 \leq q_\infty/K_s \leq 1$. If one propagates a solution upward from the water table where $\phi = 1$ ($\psi = 0$), then ϕ reaches some value corresponding to ϕ_1 at the base of a given layer. Whether ϕ increases or decreases in the overlying layer then depends upon the sign of $\phi_1 - q_\infty/K_s$ (*i.e.*, whether the potential at the base of the layer is greater or less than the unit-head-gradient value, toward which it must adjust), provided $0 \leq q_\infty/K_s \leq 1$. If the flux falls outside of these limits, (4.2) is valid only if the thickness of the overlying layer is such that $0 \leq \phi \leq 1$.

4.2 One-Dimensional Flow in a Multilayered Region

A nontrivial test problem is steady vertical flow through a layered material as was studied in the COVE 2A benchmarking exercise. The results from the analytical solution can be compared to the results obtained by Hopkins using the code LLUVIA (Hopkins, 1990; Hopkins and Eaton, 1990). The boundary conditions for these problems are a specified flux, q_0 (Table 4.1), at the top of the layered region and $\psi = \psi_0 = 0$, simulating the water table, at a 530.4 m depth. The differential equation for the potential is, in each layer,

$$\frac{d^2\phi_i}{dz^2} - \alpha_i \frac{d\phi_i}{dz} = 0 \quad , \tag{4.4}$$

where z is the vertical coordinate defined here as positive in the direction of gravity, and the subscript refers to the ith layer. In addition to satisfying the boundary conditions, the flux and pressure head must be continuous across each interface between the layers. This latter condition requires

$$(\phi_i)^{\alpha_i^{-1}} = (\phi_{i+1})^{\alpha_{i+1}^{-1}}, \quad i = 1, ..., N-1$$

for a region with N layers. Application of these matching conditions together with the boundary conditions yields the solution to (4.4) for each layer,

$$\phi_i = \frac{q_0}{K_i} + B_i e^{\alpha_i z}, \quad l_{i-1} \leq z \leq l_i \quad , \tag{4.5}$$

$$B_i = \left[\left(\frac{q_0}{K_{i+1}} + B_{i+1} e^{\alpha_{i+1} l_i} \right)^{\frac{\alpha_i}{\alpha_{i+1}}} - \frac{q_0}{K_i} \right] e^{-\alpha_i l_i}, \quad i = 1, ..., N-1 \quad , \tag{4.6}$$

$$B_N = (\phi_0 - \frac{q_0}{K_N}) e^{-\alpha_N L} \quad , \tag{4.7}$$

where ϕ_0 is the potential specified at the lower boundary, K_i is the saturated hydraulic conductivity for the ith layer, l_i is depth to the bottom of the ith layer, and $L(= l_N)$ is the depth of the entire region.

The pressure head values given by this analytical solution, using the material parameter values given in Table 3.2, are compared to the solutions obtained by Hopkins (1990) using LLUVIA in Figures 4.1 through 4.4.

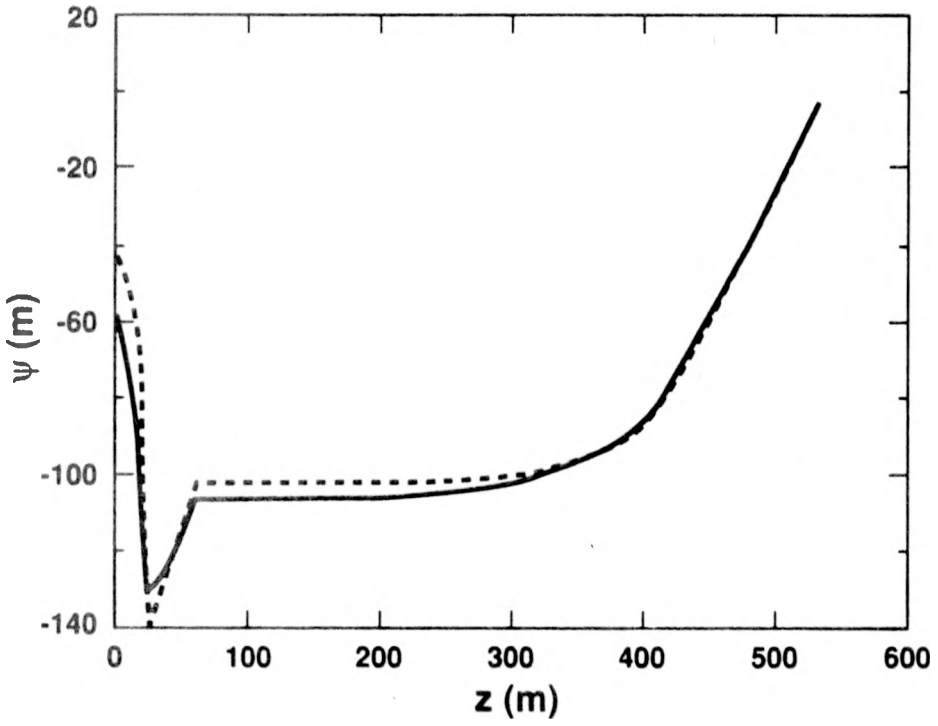

Figure 4.1. Comparison of pressure head profiles for $q_0 = 0.1$ mm/yr, and unit Chnz (Case 1 of COVE 2); —— LLUVIA, – – – quasilinear (equation 4.5).

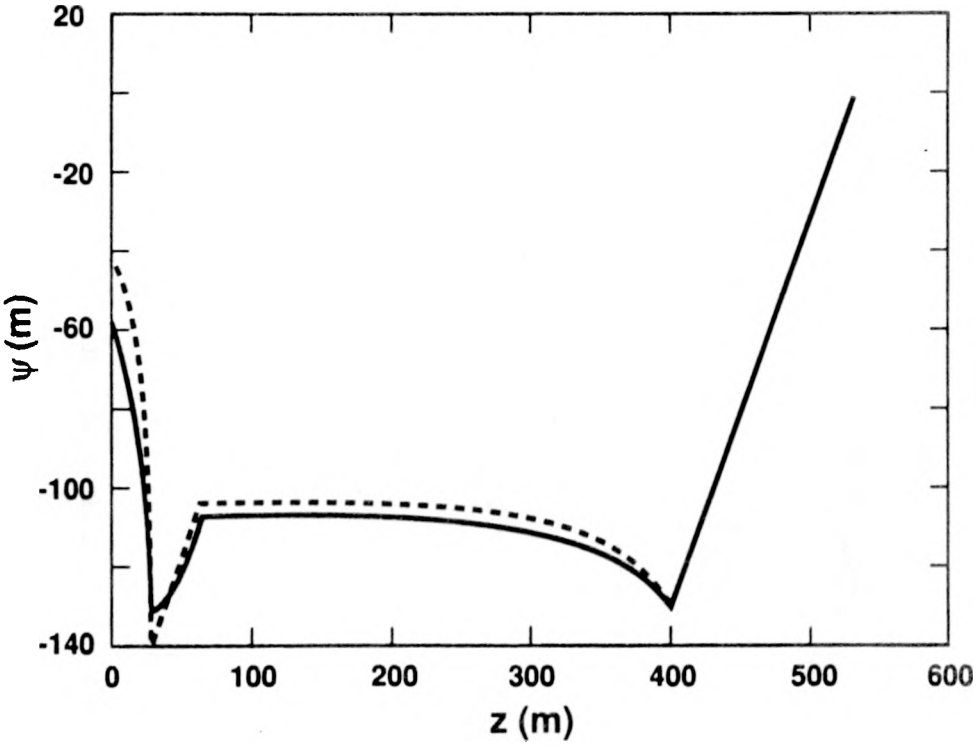

Figure 4.2. Comparison of pressure head profiles for $q_0 = 0.1$ mm/yr, and unit Chnv (Case 2 of COVE 2); —— LLUVIA, – – – quasilinear (equation 4.5).

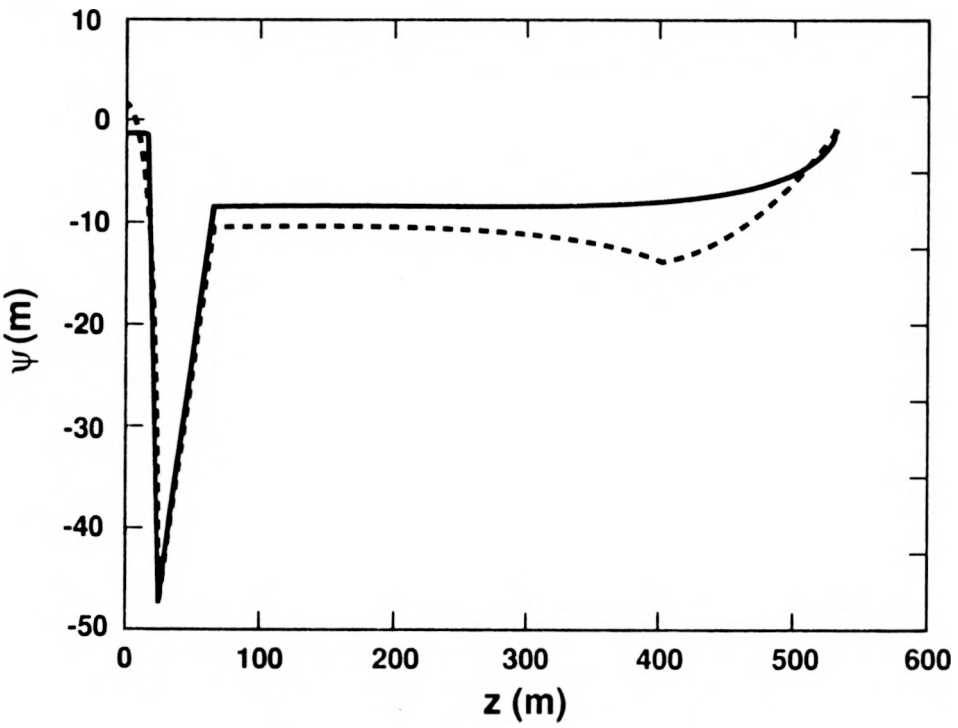

Figure 4.3. Comparison of pressure head profiles for $q_0 = 0.5$ mm/yr, and unit Chnz (Case 3 of COVE 2); — LLUVIA, – – – quasilinear (equation 4.5).

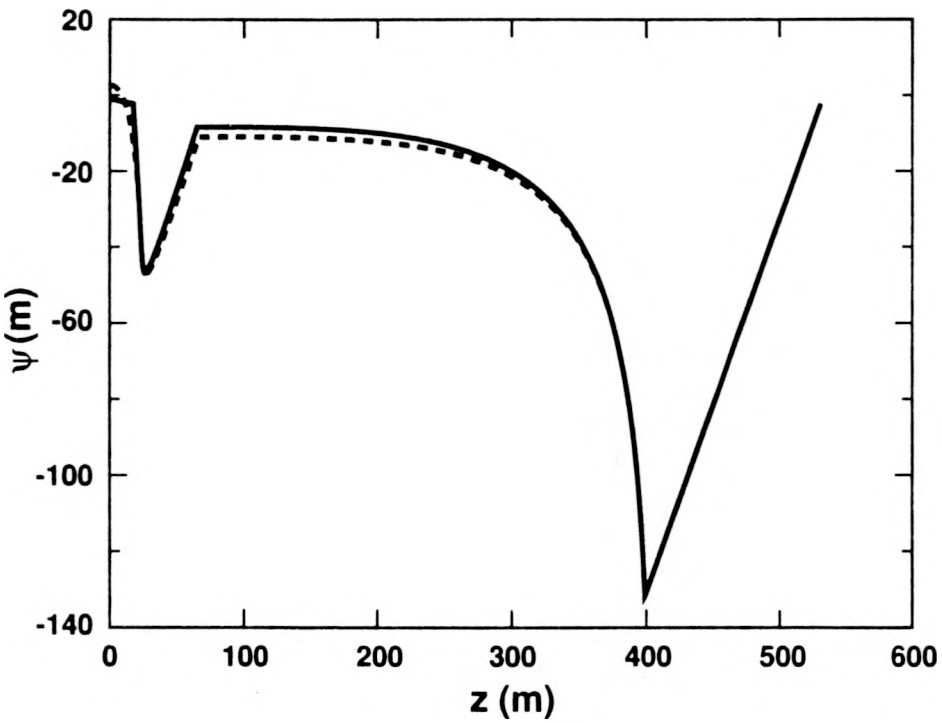

Figure 4.4. Comparison of pressure head profiles for $q_0 = 0.5$ mm/yr, and unit Chnv (Case 4 of COVE 2); —— LLUVIA, – – – quasilinear (equation 4.5).

Table 4.1. COVE 2A Test Problem Conditions.

COVE 2A Case	Flux (mm/yr)	CHn
1	0.1	zeolitic
2	0.1	vitric
3	0.5	zeolitic
4	0.5	vitric

The analytical solution provides an effective approximation, especially in light of the discrepancies between the exponential and van Genuchten representations of the hydraulic conductivity functions. It is further noted that a more judicious fitting could be attempted to give better comparison between the two methods. For example, K_i could be specified to give a better fit to data in an interval of pressure head if the pressure is constrained in a given layer. This is not pursued, however, because the purpose of this demonstration is to illustrate the effectiveness of the quasi-linear method rather than to model the van Genuchten permeability function. Even though the latter can provide a better fit to data, given that it is a three-parameter function as compared to the two parameter exponential, the advantages of a quasi-linear method are substantial. In particular, the piece-wise linear equations with nonlinear interface conditions are much easier to solve than the full nonlinear equations. Furthermore, because a free-space Green's function (fundamental solution) is known for the potential ϕ, a boundary integral method may be a very effective solution technique for two- and three-dimensional steady problems including material layers. Ultimately, an efficient solution technique for materials with spatially varying properties (homogeneous within a subregion) would be highly desirable to investigate effects of locally nonhomogeneous materials on moisture transport and, hence, on travel times.

5 The Boundary Integral Equation Method

5.1 General Considerations

A number of numerical methods are available for the solution of (2.17). Here we consider the boundary integral equation method (BIEM). The application of this method is suggested by the fact that fundamental solutions are known for (2.17) in both two and three dimensions, and by favorable previous experience with the method in various branches of mathematical physics (*e.g.*, Jawson and Symm, 1977; Cruse, 1969; Brebbia, 1978; Ingham and Kelmanson, 1984; Liggett and Liu, 1983).

A remarkable feature of boundary integral methods is the reduction of the dimension

of the problem by one, *e.g.*, a three-dimensional problem is reduced to a two-dimensional integral equation defined on the bounding surface of the original problem. This reduction in dimension is appealing in general, since the relevant geometry associated with the problem is greatly reduced, and is especially useful for semi-infinite problems and some interface problems (Liggett and Liu, 1982; Martinez and Udell, 1989). In the present study, the two-dimensional boundary-value problem is reduced to a one-dimensional boundary integral equation defined on the boundary of the original two-dimensional domain. Associated with the reduction in dimension are much simpler requirements for specifying geometry in obtaining numerical solutions, which can be a large task for domain methods on problems with complex geometry. In the BIEM, only the domain boundary is discretized; an interior grid is not required. Here we consider only two-dimensional problems, but emphasize that another attractive aspect of the approach is that its extension to three dimensions, while not necessarily easy, is straightforward.

5.2 Boundary Integral Equation Formulation

The boundary integral formulation can be motivated through Green's second identity,

$$\int_{\Omega} (G\nabla^2\Phi - \Phi\nabla^2 G)d\Omega = \int_{\Gamma} \left(G\frac{\partial\Phi}{\partial n} - \Phi\frac{\partial G}{\partial n} \right) d\Gamma \quad . \tag{5.1}$$

Here, the volume Ω is bounded by the surface Γ, and, in the classical theory, Φ and G are nonsingular in Ω. The normal derivative is defined by $\partial(\cdot)/\partial n = \nabla(\cdot)\cdot\mathbf{n}$, where $\mathbf{n}$ is the outward-pointing unit normal to the boundary. To generate the boundary integral, we use the free-space fundamental solution to (2.15) with $K^{-1}dK/d\psi = \alpha = \text{constant}$. The free-space Green's function, G, satisfies

$$\nabla_x^2 G(\mathbf{x},\mathbf{y}) - \alpha\frac{\partial G}{\partial z} = -\delta(\mathbf{x}-\mathbf{y}) \quad , \tag{5.2}$$

where ∇_x^2 denotes the Laplacian operating with respect to the position vector $\mathbf{x}$, z is the vertical coordinate, positive in the direction of gravity, and δ is the Dirac delta function. The physical interpretation of the Green's function is that it represents the response at $\mathbf{x}$ due to a unit source acting at location $\mathbf{y}$. The two-dimensional solution is given by Carslaw and Jaeger (1978, p. 267) as the solution for a line source of unit strength placed at the origin:

$$G(\mathbf{x}) = \frac{1}{2\pi}\exp\left(\frac{\alpha z}{2}\right) K_0\left(\frac{\alpha r}{2}\right) \quad , \tag{5.3}$$

where $r^2 = x^2 + z^2$, and K_0 is the modified Bessel function of the second kind of order zero. The boundary integral equation (BIE) results if we substitute the free-space Green's function (5.3), generalized for the source placed at an arbitrary point $\mathbf{y} = (\chi,\zeta) \in \Omega$, into (5.1). Noting that with respect to $\mathbf{y}$, the Green's function satisfies the adjoint to equation (5.2),

$$\nabla_y^2 G(\mathbf{x},\mathbf{y}) + \alpha\frac{\partial G}{\partial \zeta} = -\delta(\mathbf{x}-\mathbf{y}) \quad ,$$

substitution of (5.3) into Green's identity, applied with respect to the source point $\mathbf{y}$, gives

$$\Phi(\mathbf{x}) + \int_\Gamma \frac{\partial G(\mathbf{x},\mathbf{y})}{\partial n}\Phi(\mathbf{y})d\Gamma(\mathbf{y}) = \int_\Gamma G(\mathbf{x},\mathbf{y})[-q_n(\mathbf{y})]d\Gamma, \quad \mathbf{x}\in\Omega \quad , \tag{5.4}$$

where $q_n(\mathbf{y}) = -\partial\Phi/\partial n + \alpha\Phi n_z$ is the flux normal to the boundary surface Γ, and $n_z = \mathbf{n}\cdot\mathbf{e_z}$ is the vertical component of the normal to Γ. This identity gives the value of the potential at any point in Ω, if the boundary values of potential and flux are known. However, in a well-posed boundary value problem, either the potential or flux (or some combination of these) is specified and the other is to be determined. A boundary integral equation can be formulated for these unknowns by taking the limit $\mathbf{x}\rightarrow\Gamma$ from Ω; the limit is indicated because the flux kernel $\partial G/\partial n$ suffers a jump as $\mathbf{x}$ passes to the boundary from the interior. The resulting BIE, applied to a smooth point $\mathbf{x}$ on the boundary (*i.e.*, one having a well-defined local tangent plane) is the same as equation (5.4) if we multiply the first term on the left-hand side by 1/2. Pullan and Collins (1987) show the values taken on by the principal value when $\mathbf{x}$ is on a corner of the boundary.

5.3 Numerical Solution

In this preliminary investigation of the quasi-linear method the simplest of numerical approximations is used in order to facilitate coding of the algorithm. Higher order approximations (Pullan and Collins, 1987; Martinez and Udell, 1989) can be incorporated later if deemed necessary. The first step in the numerical approximation of (5.4) is to discretize the boundary Γ into a number of boundary elements, Γ_n ($n = 1,..,N$). In the present version, the boundary elements are all straight line segments. Next, the variation of Φ and q_n over each segment is approximated by its value at the center of the boundary element, hence the numerical approximation to the BIE becomes

$$\frac{1}{2}\Phi(\mathbf{x}_i) + \sum_j \Phi_j G'_{ij} = \sum_j (-q_{nj})G_{ij} \quad , \tag{5.5}$$

where $\Phi_j = \Phi(\mathbf{x}_j)$, $q_{nj} = q_n(\mathbf{x}_j)$, and

$$G'_{ij} = \int_{\Gamma_j} \frac{\partial G(\mathbf{x}_i,\mathbf{y})}{\partial n} d\Gamma(\mathbf{y}) \quad ,$$

$$G_{ij} = \int_{\Gamma_j} G(\mathbf{x}_i,\mathbf{y})d\Gamma(\mathbf{y}) \quad .$$

For purposes of computing the coefficients, it is convenient to describe the geometry parametrically. In the present method we write

$$\mathbf{y} = \begin{pmatrix} \chi \\ \zeta \end{pmatrix} = \sum_{k=1}^{2} \begin{pmatrix} N_k\chi_k \\ N_k\zeta_k \end{pmatrix} \tag{5.6}$$

with Lagrange interpolants

$$\begin{pmatrix} N_1 \\ N_2 \end{pmatrix} = \frac{1}{2} \begin{pmatrix} (1-\xi) \\ (1+\xi) \end{pmatrix} \quad . \tag{5.7}$$

The endpoint coordinates for the boundary elements are (χ_k, ζ_k) and ξ is the parametric distance along the element, defined such that $-1 \leq \xi \leq 1$. An element of surface is given by

$$d\Gamma = J d\xi, \quad J = (\chi_\xi^2 + \zeta_\xi^2)^{\frac{1}{2}} \quad .$$

In the present formulation, with straight-sided elements, the Jacobian is simply half the length of the element, $J = ((\chi_1 - \chi_2)^2 + (\zeta_1 - \zeta_2)^2)^{\frac{1}{2}}/2$, where the subscripts refer to the endpoints of a particular boundary element.

If this parameterization of the geometry is used, a general numerical algorithm can be written to compute the coefficients for a general boundary element, *e.g.*,

$$G_{ij} = \int_{-1}^{1} G[\mathbf{x}_i, \mathbf{y}(\xi)] J_j d\xi \quad ,$$

with a similar expression for G'_{ij}. The coefficients G_{ij} and G'_{ij} are computed using four-point Gauss-Legendre quadrature. When $x_i \in \Gamma_j$ the kernels are improper, because of the singular nature of the Green's function when $\mathbf{x} = \mathbf{y}$, and these coefficients are computed by subtracting the singularity, integrating it analytically, and summing with the numerical integral of the remainder. In particular, $G \to G_\epsilon$, as $\mathbf{x} \to \mathbf{y}$, where

$$G_\epsilon = -\ln\left(\frac{\alpha}{2} J|\xi|\right).$$

Hence, to compute G_{ii}, we write

$$G_{ii} = \int_{\Gamma_i} \{G[\mathbf{x}_i, \mathbf{y}(\xi)] - G_\epsilon[\mathbf{x}_i, \mathbf{y}(\xi)]\}\, d\Gamma[\mathbf{y}(\xi)] + \int_{\Gamma_i} G_\epsilon[\mathbf{x}_i, \mathbf{y}(\xi)] d\Gamma[\mathbf{y}(\xi)] \quad .$$

Now, the first integral is regular as $\mathbf{x} \to \mathbf{y}$, and can be computed accurately by four-point Gauss-Legendre quadrature, and the last integral is given by

$$\frac{J}{\pi}\left[\left(\frac{\alpha}{2}J\right)^{-1} + 1\right] \quad . \tag{5.8}$$

When we apply the boundary integral equation to each of the N boundary elements, use the boundary conditions (which specify half of the $2N$ point values of potential and flux), and rearrange, we get the linear system $\mathbf{A}\mathbf{u}_h = \mathbf{f}$ where $\mathbf{u}_h$ contains the unknown potential or flux on the boundary and $\mathbf{f}$ contains the inner product of specified boundary values (*i.e.*, boundary conditions) and kernel coefficients. Once the boundary values are determined by solving the linear system by Gaussian elimination, the BIE (5.4) can be

used to compute the potential at any interior point. The flux vector in the interior can also be computed by operating on (5.4) according to

$$\mathbf{q}(\mathbf{x}) = -\nabla\Phi + \alpha\Phi\nabla z \quad . \tag{5.9}$$

The explicit statement of the flux, formed from (5.4) and (5.9), is given in Appendix A.

Pathlines can also be computed once the flux vector has been determined. Pathlines are computed by numerically integrating the equations

$$\frac{d}{dt}\begin{pmatrix} x \\ z \end{pmatrix} = \begin{pmatrix} v_x \\ v_z \end{pmatrix} = \frac{1}{\theta}\begin{pmatrix} q_x \\ q_z \end{pmatrix}$$

for each pathline, subject to an initial coordinate location (x_o, z_o). The moisture content must be specified as a function of pressure head, $\theta(\psi)$, to determine the interstitial velocity, $\mathbf{v}$ $(=\mathbf{q}/\theta)$, according to the Dupuit assumption. In this way, both the particle path and the elapsed time for the particle to traverse a given distance along the path can be determined.[2]

6 Convergence

The preliminary version of the code described in the foregoing was written to allow rapid numerical solutions for assessing the utility of the quasi-linear method. Hence the program was written using the simplest of numerical approximations to facilitate the coding of the algorithm. Among these is the use of the "constant element" as the basis set for the unknowns. Constant elements approximate the variation of the unknown on each element by its value at the middle of the element, a somewhat lower-order interpolant. Nevertheless, we found that on problems with smoothly varying solutions, the convergence was quadratic with boundary element size reduction; *i.e.*, doubling the number of elements on a uniform mesh reduces the solution error by one-fourth. However, this convergence rate is degraded significantly when there are singularities in the problem.

Singularities can arise quite often in practice; some are inherent in the boundary integral formulation. Corners and ends can result in singularities, especially when the boundary conditions also change type at the same location. Flux boundary conditions can also result in singularities at corners because they depend linearly on the surface normal, which is discontinuous there. Usually, these can be avoided by using elements that do not place node points on these corners (*e.g.*, constant elements) or that use basis functions that incorporate the singular behavior (Ingham and Kelmanson, 1984; Pullan and Collins, 1987). More generally, singularities can also arise from a step change in boundary condition type on a line, as we consider here. This singularity can also be addressed by incorporating the local behavior in the basis function. However, recent

[2]If only the pathline is desired, without regard for the travel time, it is computationally expedient to integrate the single equation $dz/dx = v_z/v_x$ for each pathline rather than the pair indicated above.

work (Yan and Sloan, 1989) indicates that this problem can be treated effectively by appropriate mesh grading near the singularity. We present results using the mesh grading algorithm suggested by Yan and Sloan (1989) for a similar problem as considered below. We find that the quadratic convergence seen in test problems (see, *e.g.*, Section 7.1) can be restored by mesh grading.

6.1 Problem Statement

In connection with the distribution of moisture beneath a two-dimensional surface source,[3] we consider the boundary-value problem,

$$\nabla^2 p - a\frac{\partial p}{\partial z} = 0 \quad , \tag{6.1}$$

subject to the following boundary conditions on the surface,

$$p = 1, \quad |x| < 1, \quad z = 0 \quad , \tag{6.2}$$

$$-\frac{\partial p}{\partial z} + ap = 0, \quad |x| > 1, \quad z = 0 \quad , \tag{6.3}$$

and the far-field condition,

$$p \to 0, \quad \mathbf{x} \to \infty \quad . \tag{6.4}$$

This boundary value problem describes the infiltration of moisture into a porous half-space from a strip source. In this coordinate system, z is the vertical coordinate, which increases in the direction of gravity. Numerical solutions are obtained, for various values of the parameter a, by applying the BIEM via the "constant element" code described in Section 5. The far-field condition is inherent in the Green's function formulation of the BIEM, and hence this condition is automatically satisfied far from the surface. Hence, boundary elements are placed only along the surface ($z = 0$) over some distance $|x| \leq L$. We note that the solution is symmetric with respect to $x = 0$, and hence we could halve the number of unknowns by applying symmetry. We did not exploit this symmetry, however, because the CPU requirements are modest enough that we found it easier simply to use elements over $-L \leq x \leq L$ (twice as many elements as are necessary).

The singularity arises because of the step change in boundary condition type, from Dirichlet to flux, at $|x| = 1$. The variation in potential p and normal flux $q_n = -\partial p/\partial z + ap$ along the surface are shown in Figures 6.1 and 6.2, respectively, for $a = 1$. Although the potential does decrease rapidly beyond $x = 1$, it is the flux that exhibits the singular behavior near $x = 1$. Physically, this singularity models the large lateral gradient in potential owing to the change from a specified potential to an impermeable surface at $x = 1$.

[3]We defer detailed discussion of this problem to a companion report: Martinez, M. J., and D. F. McTigue, The distribution of moisture beneath a two-dimensional surface source, *Sandia National Laboratories Technical Report*, **SAND90-0252**, February, 1991.

6.2 Mesh Grading

Recent work by Yan and Sloan (1989) on a similar problem indicates that singularities can be treated effectively by mesh grading. Yan and Sloan consider integral equations with logarithmic kernels, as arise in potential problems. The kernel for the BIEM reformulation of the seepage problem above is given in equation (5.3). The Bessel function $K_0(\xi)$ also has a logarithmic singularity for $\xi \to 0$, and hence the mesh grading may be useful here.

The mesh grading algorithm analyzed by Yan and Sloan was actually proposed by Rice (1969) and Chandler (1984). The algorithm places the mesh points, x_i, over the interval $s_0 \leq x \leq s_1$, according to,

$$x_i = s_0 + \frac{1}{2}\left(\frac{i}{n}\right)^{\eta}(s_1 - s_0), \quad 0 \leq i \leq n \quad , \tag{6.5}$$

and

$$x_i = s_1 - \frac{1}{2}\left(\frac{2n - i}{n}\right)^{\eta}(s_1 - s_0), \quad n \leq i \leq 2n \quad , \tag{6.6}$$

where η is a positive real number, and $2n$ nodes are places over the interval. The algorithm increases the density of the nodes near the endpoints $x = s_0$ and $x = s_1$. This is actually a special case of a more general algorithm where mesh points are placed along a curvilinear portion of the boundary, rather than along the straight line proposed here. This simplification is sufficient to illustrate the mesh grading without sacrificing any essential feature. The analysis of Sloan and Spence (1988) indicates that, for an open surface as considered here, the error norm on a uniform mesh behaves as,

$$||g_h - g||^2 = O(h \log h^{-1}) \quad , \tag{6.7}$$

where g_h denotes the numerical solution, g the exact solution, and h is the element size. As noted before, these analyses are for potential problems formulated as integral equations of the first kind, however the quasi-linear seepage problems exhibits a similar kernel behavior. The error norm is defined by

$$||g||^2 = (Kg, g), \quad (f, g) = \int_{\Gamma} f(y)g(y)d\Gamma(y) \quad , \tag{6.8}$$

and Kg is the operator form of the boundary integral equation considered in (Yan and Sloan, 1989; Sloan and Spence, 1988),

$$(Kg)(x) = -\int_{\Gamma} \log|x - y|g(y)d\Gamma = f(x) \quad , \tag{6.9}$$

where $f(x)$ are the boundary values of potential (given). By using the mesh grading, Yan and Sloan show that the convergence rate can be restored to higher order. In particular, they show that (see Theorem 3.1 of Yan and Sloan) if $\eta = 2$,

$$||g_h - g||^2 = O[h^2(\log h^{-1})^2] \quad , \tag{6.10}$$

and if $\eta \geq 4$

$$||g_h - g||^2 = O(h^3 \log h^{-1}) \quad . \tag{6.11}$$

Table 6.1. Error analysis for uniform meshes ($\eta = 1$).

$N_s = h^{-1}$	N_T	F_{oh}	E_{abs}	E_{rel}	k
1	22	2.94037	0.28398	8.81 (-2)	–
2	44	3.06725	0.15710	4.87 (-2)	0.854
4	88	3.14180	0.08255	2.56 (-2)	0.928

6.3 Numerical Results

The numerical results to follow are all for $a = 1$; solutions for arbitrary a can be found in the report cited on page 33. The extent of the mesh was $|L| = 20$, which, as illustrated in Figures 6.1 and 6.2, is sufficient to eliminate end effects. This value was determined by trial and error.

In Table 6.1 we show the convergence rate for mesh size reduction on uniform meshes. In Tables 6.1 through 6.4, N_s indicates the number of elements used over half the source region, *e.g.*, $0 \leq x \leq 1$, and N_T is the total number of elements over $-L \leq x \leq L$, including $2N_s$. The mesh spacing was uniformly halved in arriving at the convergence results of Table 6.1. For the mesh grading results, the mesh was graded according to (6.5) and (6.6) above, with nodes clustered symmetrically about $|x| = 1$ over $0 \leq |x| \leq 2$. The mesh grading was continued beyond $|x| = 2$ using (6.5). The absolute error definition which is closest in form to the definition used by Yan and Sloan is given by

$$E_{abs} = |F_0 - F_{0h}| \quad , \tag{6.12}$$

where F_{0h} is the numerical nondimensional flux through the source area. Ideally, F_0 should be the exact value, however since this is an unknown, we use the converged numerical value for $\eta = 3$, and $N_s = 16$, given in Table 6.3. The relative error, E_{rel}, is defined by $E_{rel} = E_{abs}/F_0$, and k is the convergence rate, *i.e.*,

$$E_{abs} = ch^k \quad , \tag{6.13}$$

where $h = N_s^{-1}$ for present purposes and c is a constant independent of h. Table 6.1 indicates that the convergence rate is slightly sublinear for uniform mesh reduction. This agrees with the analyses of Yan and Sloan (1989) and Sloan and Spence (1988), expressed in (6.7), for the potential problem. In spite of the low convergence rate, the algorithm yields rather good results on coarse meshes for a singular problem. The mesh using only 2 elements over the entire source region ($N_s = 1$) gives a flux with about 9% error.

Tables 6.2 through 6.4 list the results using mesh grading for $\eta = 2$, 3, and 4, respectively. Quadratic convergence is restored with mesh grading, as predicted by Yan and Sloan. However, the improvement to cubic convergence with $\eta = 4$ is difficult to confirm from Table 6.4. In fact the "exact" value of F_0 was chosen from Table 6.3, and not

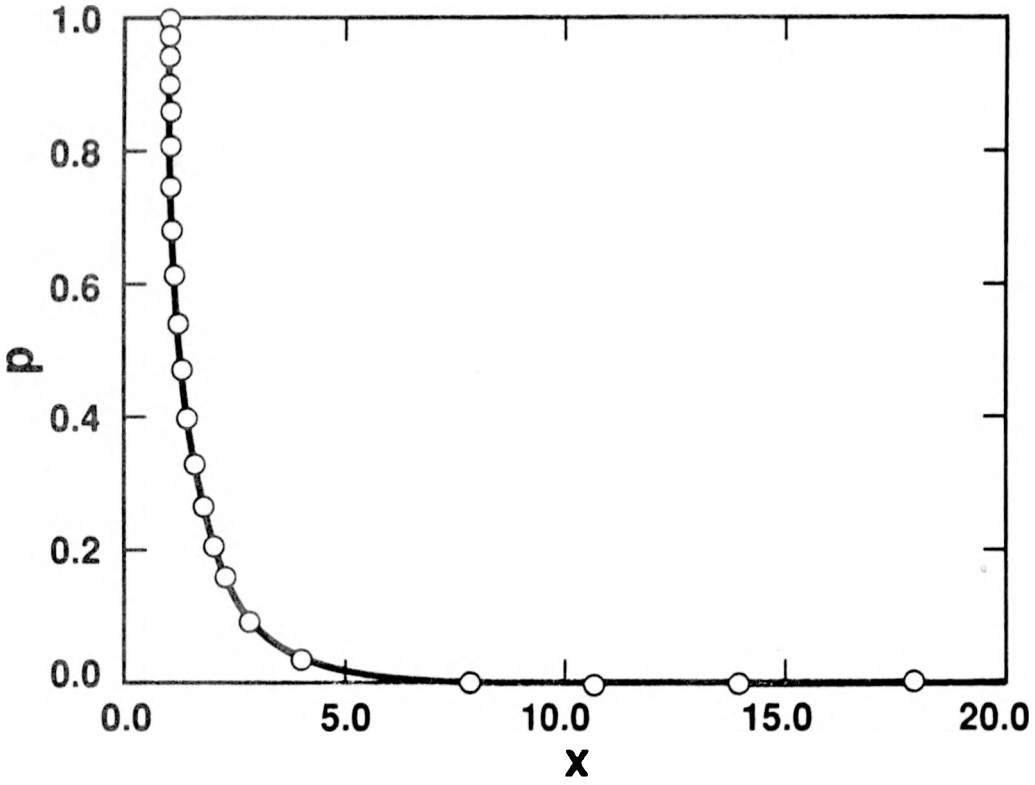

Figure 6.1. Variation of potential along the surface $z = 0$, for $a = 1$.

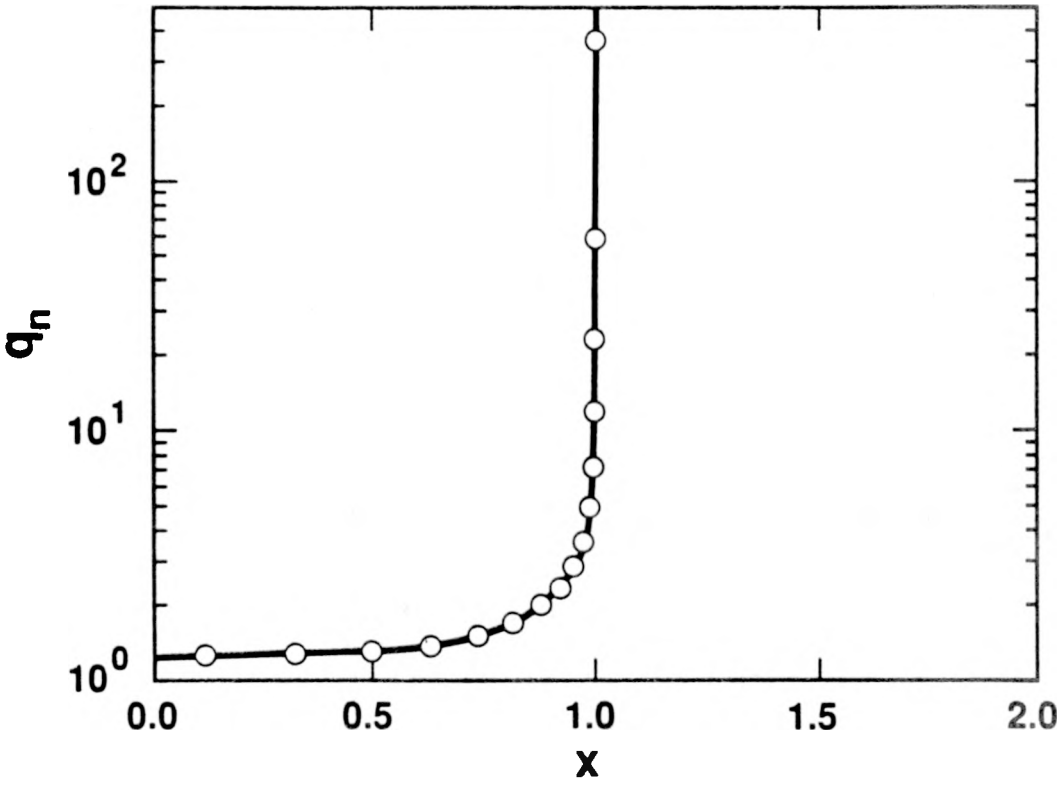

Figure 6.2. Variation of normal flux along the surface $z = 0$, for $a = 1$.

from Table 6.4, because numerical values in the former appear to have better accuracy for $N_s \leq 8$ with respect to either of the numerical values for $N_s = 16$ in Tables 6.3 and 6.4. The convergence rates in Tables 6.2 and 6.4, for $N_s = 16$ are likely inaccurate because we do not know the exact value, and these entries compare numerical values obtained with the same resolution as the numerical F_0 from Table 6.3 used as the "exact" value.

Table 6.2. Error analysis for graded meshes ($\eta = 2$).

$N_s = h^{-1}$	N_T	F_{oh}	E_{abs}	E_{rel}	k
2	16	3.12933	0.09502	2.95 (-2)	–
4	28	3.19714	0.02722	8.44 (-3)	1.80
8	48	3.21775	0.00661	2.05 (-3)	2.04
16	86	3.22374	0.00062	1.91 (-4)	3.42

Table 6.3. Error analysis for graded meshes ($\eta = 3$).

$N_s = h^{-1}$	N_T	F_{oh}	E_{abs}	E_{rel}	k
2	16	3.14820	0.07616	2.36 (-2)	–
4	28	3.20653	0.01782	5.53 (-3)	2.09
8	48	3.22132	0.00303	9.41 (-4)	2.55
16	86	3.22436	–	–	–

Table 6.4. Error analysis for graded meshes ($\eta = 4$).

$N_s = h^{-1}$	N_T	F_{oh}	E_{abs}	E_{rel}	k
2	16	3.14220	0.08215	2.55 (-2)	–
4	28	3.20491	0.01945	6.03 (-3)	2.08
8	48	3.22093	0.00343	1.06 (-3)	2.50
16	86	3.22425	0.00011	3.38 (-4)	4.97

This approach to treating singular problems with the BIEM is simple and effective. In addition, the number of boundary elements required to achieve a certain error level is much reduced using mesh grading. However, it appears that, based on these limited numerical results, quadratic convergence is about all that can be obtained from mesh grading for the quasi-linear boundary integral analysis using constant elements. Futhermore, the use of $\eta = 2$ in the mesh grading algorithm is sufficient to obtain quadratic convergence.

7 Test Problems

In this section, we present results from two boundary-value problems considered as test cases for the BIEM code described in Sections 5 and 6. First, we show comparisons to an exact, analytical solution in a two-dimensional domain. The second test problem involves a comparison between solutions obtained with the BIEM code and with an existing finite-element code that solves the full, nonlinear problem. The latter problem assumes material properties typical of tuffs from Yucca Mountain.

7.1 Comparison to an Exact Solution in Two Dimensions

The code written to perform the numerical approximations using the BIEM was tested by comparing to some one- and two-dimensional problems with known analytical solutions. Both Dirichlet and flux boundary conditions have been tested satisfactorily. Some selective error analyses indicate approximately quadratic convergence with boundary element size reduction.

The two-dimensional test problem is to solve (2.17) with Dirichlet conditions specified on the boundaries of the unit square. A contrived analytical solution for this problem is constructed as a product of two Fourier terms in a series solution,

$$\phi(x,z) = e^{mz}\cos(\frac{\pi}{2}x), \quad m = \frac{\alpha}{2} - \sqrt{(\frac{\alpha}{2})^2 + (\frac{\pi}{2})^2} \quad . \tag{7.1}$$

The specified values of ϕ on the boundaries for the numerical solution are computed from (7.1). Figure 7.1 compares contours of potential (ϕ) obtained with the BIE code, using 12 boundary elements (3 nodes per side), with the analytical values for $\alpha = 0.1$. The comparison is excellent. Figure 7.2 compares profiles of potential along the vertical direction obtained with the BIEM code (12 boundary nodes) with the analytical solution. Error analysis at selected points indicates the error in the BIEM solution, using 3 nodes per side, is less than 1% everywhere. A simulation using flux boundary conditions on part of the boundary also compared well with the analytical solution.

The deviation of the BIEM solution near the boundaries ($z = 0$ and $z = 1$) in Figure 7.2 shows that computation of interior values very near the boundaries can result in large numerical error. As a rule, if an interior point computation is requested at a place closer to the boundary than the local spacing between boundary nodes, the calculation should use interpolation. That is, the interior value is computed at an appropriate distance from the boundary and the requested value computed by interpolation using the interior value and the local boundary values.

7.2 Comparisons to Finite-Element Solutions for Tuff

To examine the viability of the quasi-linear method for the Yucca Mountain Project, some representative two-dimensional problems were examined. In these test problems we

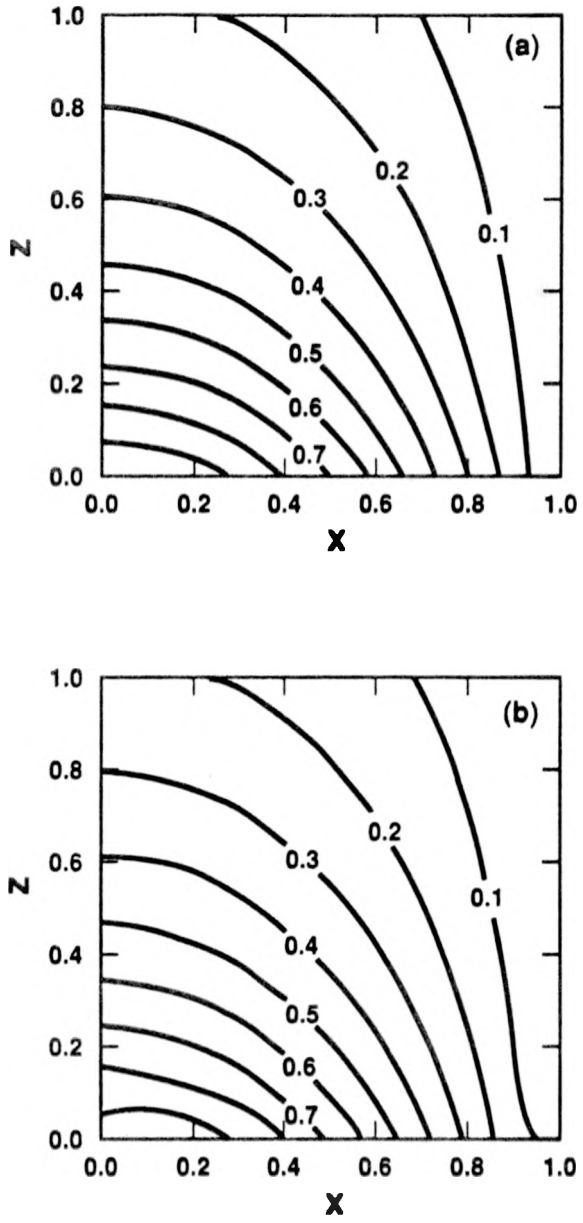

Figure 7.1. Isopotentials in the unit square; (a) analytical values; (b) numerical values.

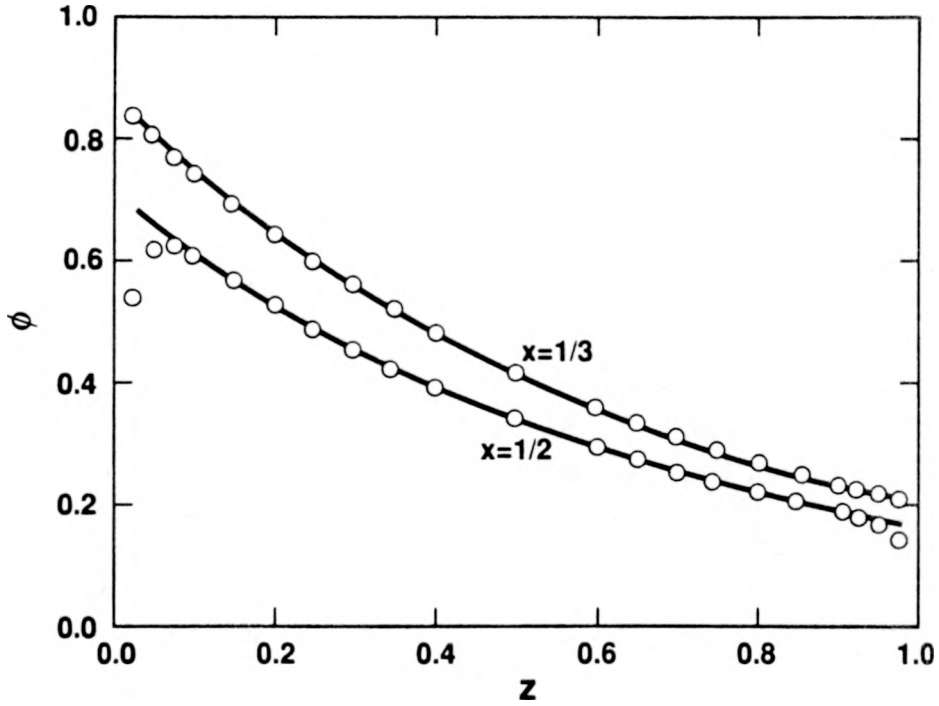

Figure 7.2. Comparison of profiles of potential along the vertical direction for $x = 1/3$ and $x = 1/2$. The curves represent the analytical solution and the symbols are the numerical values.

consider the steady unsaturated flow in the box shown in Figure 7.3. The dimensions of the box, 100 m by 100 m, were chosen to be of the order of α^{-1} for the materials of interest so that the pressure-gradient and body-force terms of equation (2.17) are of the same order. Dirichlet conditions are specified along the upper surface and along one-fourth of the lower boundary. Impermeable conditions are specified on the remainder of the boundary. Material properties (Hopkins, 1990) representative of the Topopah Spring (TSw) and Calico Hills (CHnv) units of Yucca Mountain are considered, and are designated Case 1 and Case 2, respectively (Table 7.1). In each case, we carry out the simulation using both the van Genuchten/Mualem model and the exponential model. The comparison of these two representations of permeability was shown previously in Figures 3.3 and 3.4. As noted in Section 3.1, the two permeability representations compare well for Topopah and poorly for Calico Hills.

We compare solutions to the boundary-value problem illustrated in Figure 7.3 generated with the BIEM and with the finite-element code NORIA (Bixler, 1985). Conditions for the problems are given in Table 7.1. Solutions using both the exponential and the van Genuchten representation were generated with NORIA. The purpose was twofold: (1) to compare the solutions using the exponential representation in NORIA with the BIEM (providing a benchmark for latter); and (2) to compare the van Genuchten and exponential permeability models.

The conditions for Case 1 allow comparison of the quasi-linear transformation for solving the non-linear problem with solutions generated by NORIA using the Richards equation. In this case, because the exponential conductivity function is essentially identical to the van Genuchten representation, one might anticipate that the results based on either model or either solution method would be very similar. Case 2 was chosen to test a material and a range of pressure head for which the two conductivity functions are markedly different. The pressure boundary conditions for Case 2, $\psi = -25$ m at the outlet and $\psi = -75$ m at the top, straddle the steep drop in permeability with pressure head represented by the van Genuchten model (Figure 3.4). The conductivity for the exponential model is thus underestimated at values of $|\psi|$ below about 50 m, and overestimated at values of $|\psi|$ above that level.

Contour plots of pressure head for Case 1 are shown in Figure 7.4a for the van Genuchten permeability and in Figure 7.4b for the exponential, both generated using NORIA. The pressure fields are nearly identical for this case, because both permeability functions are also nearly identical in this pressure head range. Figures 7.5 through 7.8 compare pressure head and flux profiles along the vertical obtained using NORIA with those obtained using the BIEM. The figures demonstrate that the quasi-linear method yields the same results as NORIA for this case. The BIEM solutions were obtained using 32 boundary elements (8 evenly spaced nodes per side). Solutions using 16 boundary elements, the minimum number of evenly spaced nodes to allow one boundary element on the Dirichlet segment of the lower boundary, yielded results with less than 1% difference.

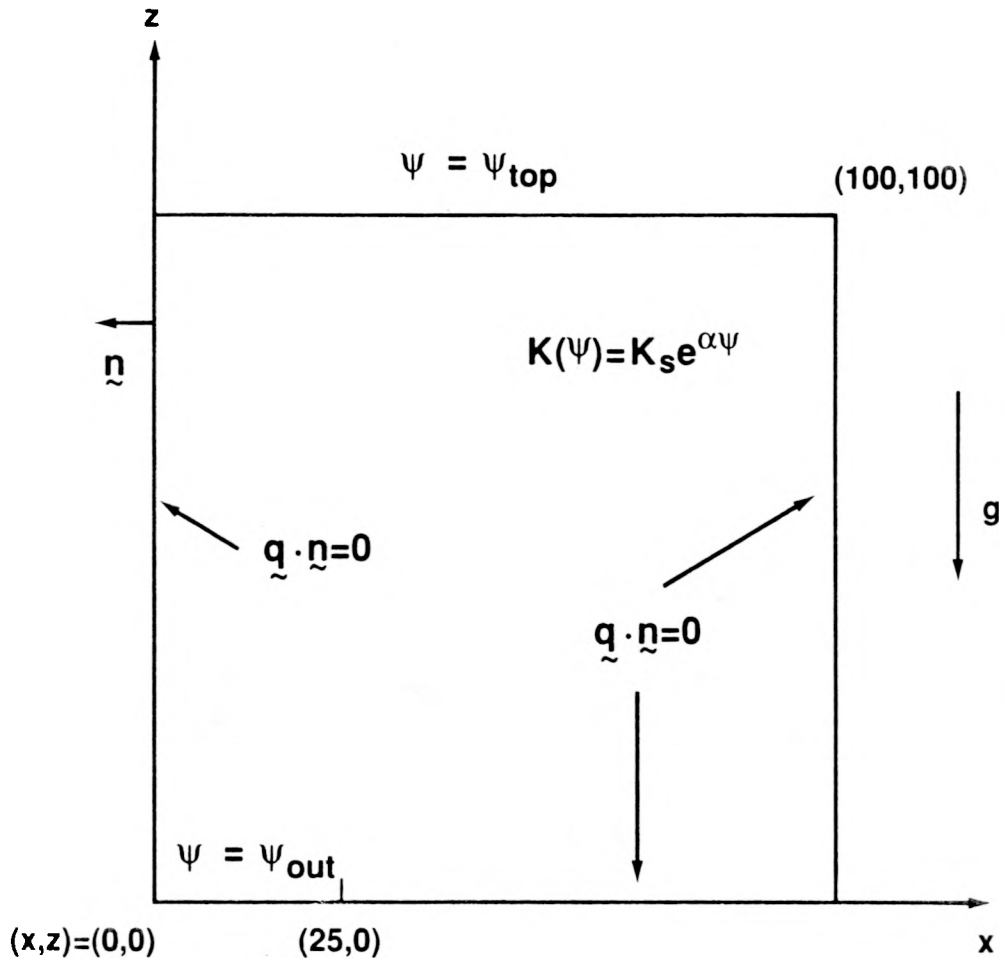

Figure 7.3. Schematic of the test problem using Yucca Mountain properties.

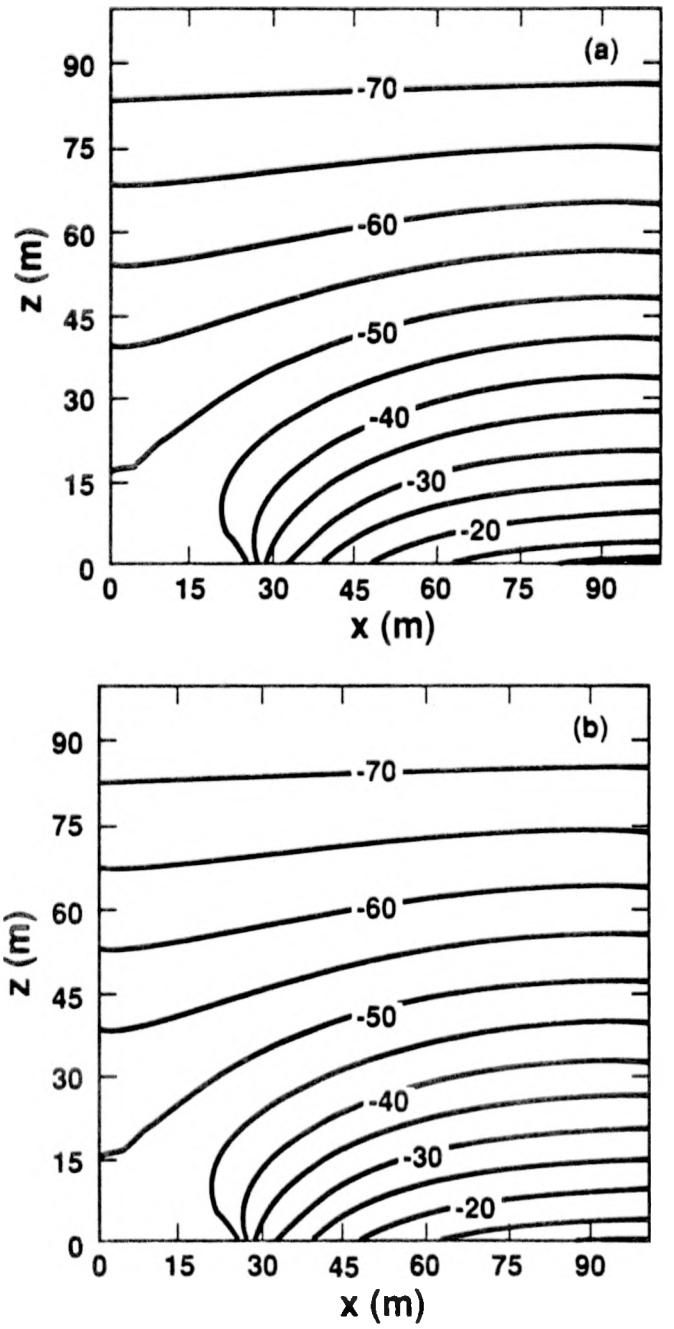

Figure 7.4. Contours of pressure head for Case 1 using (a) the van Genuchten/Mualem permeability model, and (b) the exponential permeability model.

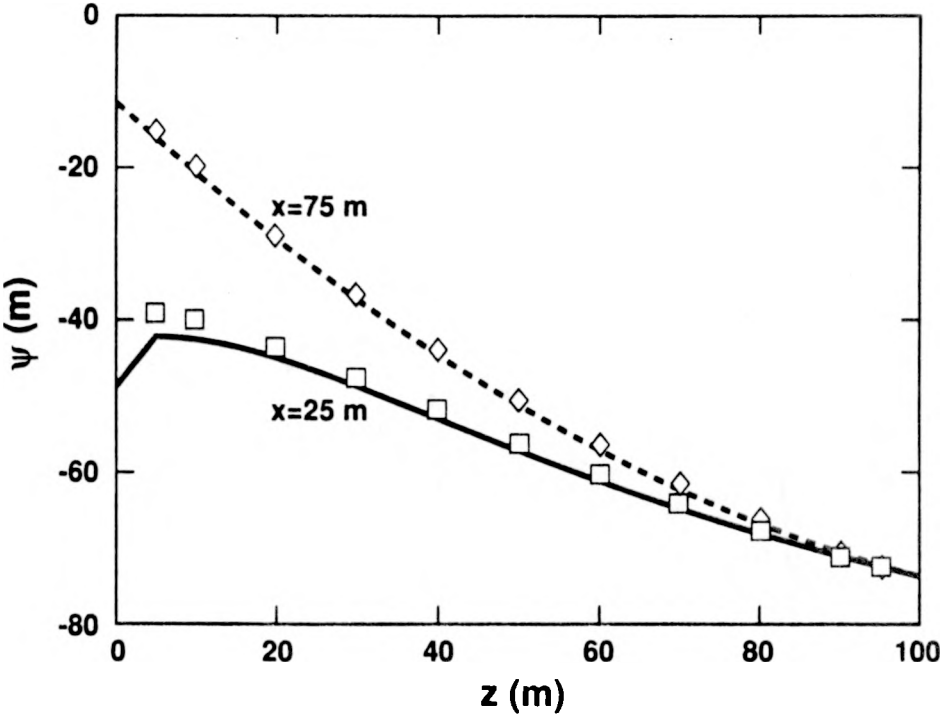

Figure 7.5. Comparison of pressure head profiles along the vertical direction using the exponential permeability in NORIA (curves) with the BIEM (symbols).

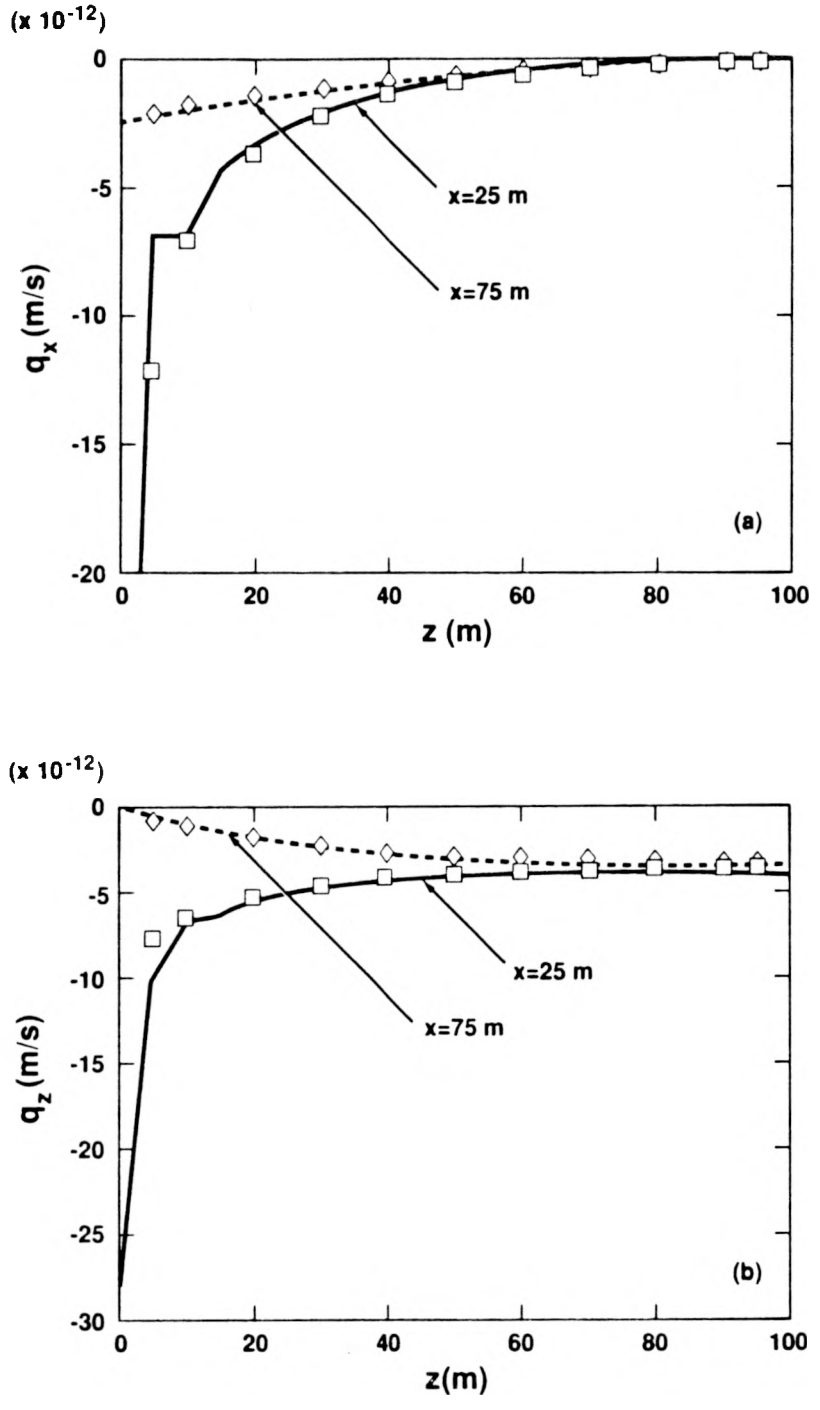

Figure 7.6. Comparison of flux profiles along the vertical direction using the exponential permeability in NORIA (curves) with the BIEM (symbols); (a) horizontal flux, (b) vertical flux.

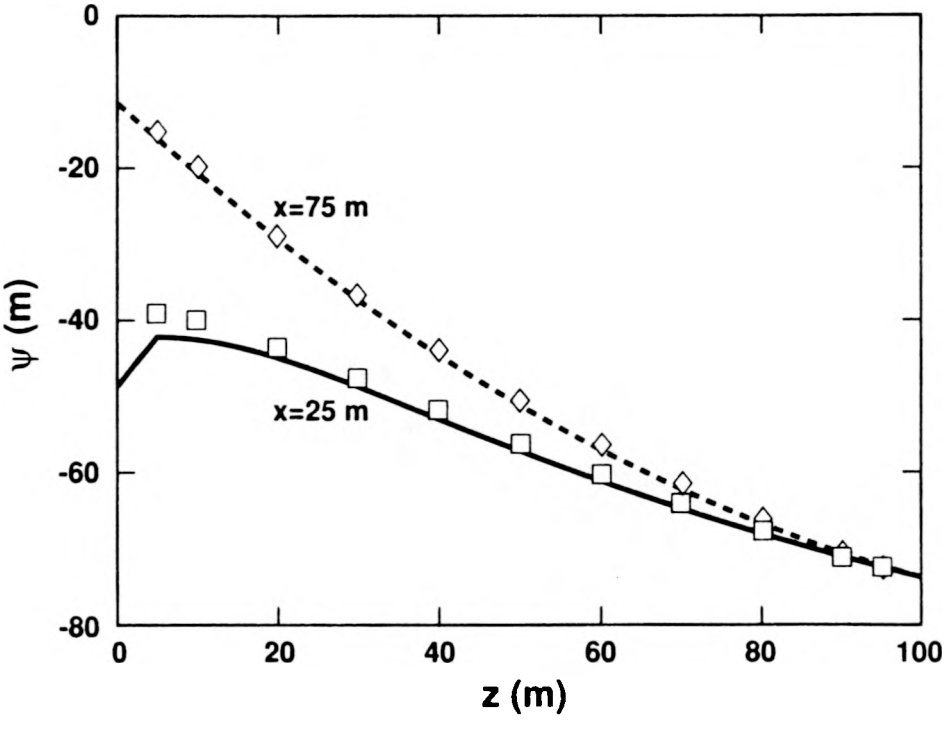

Figure 7.7. Comparison of pressure head profiles along the vertical direction using the van Genuchten permeability in NORIA (curves) with the BIEM (symbols).

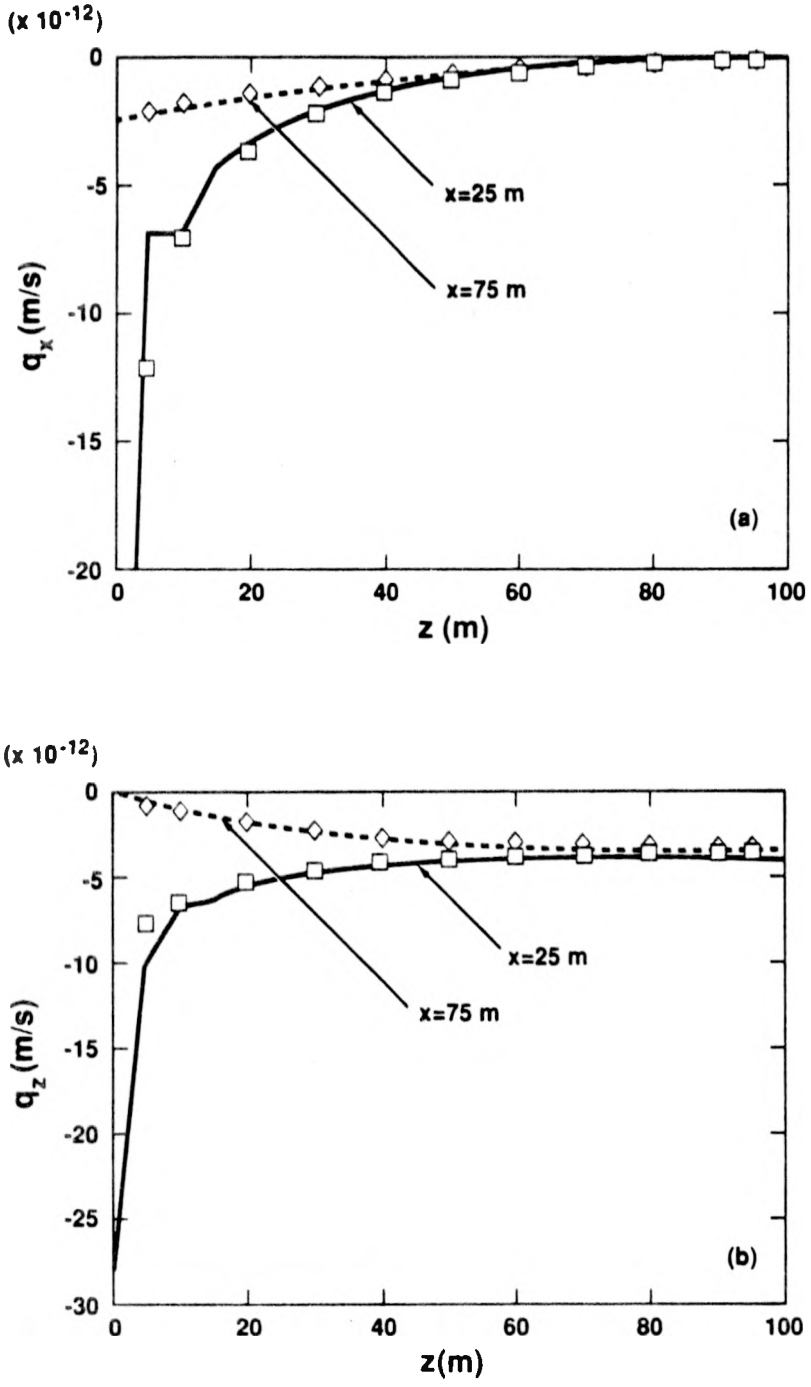

Figure 7.8. Comparison of flux profiles along the vertical direction using the van Genuchten permeability in NORIA (curves) with the BIEM (symbols); (a) horizontal flux, (b) vertical flux.

Table 7.1. Conditions for test problems.

		Boundary ψ (m)			Exponential Model	van Genuchten Model	
Case	Unit	Top	Outlet	K_s (m/s)	α (m^{-1})	α_v (m^{-1})	β
1	TSw	−75	−50	1.9×10^{-11}	0.01742	0.0567	1.798
2	CHnv	−75	−25	2.7×10^{-7}	0.02219	0.0160	3.872

Figure 7.9 compares the pressure head contours for Case 2 using the van Genuchten and exponential permeability functions in NORIA. This case specifies boundary pressures that accentuate the differences in the permeability functions. The pressure head contour maps are significantly different, as could be expected by the discrepancy in the permeability functions over this range of pressure head. Figures 7.10 and 7.11 compare the results obtained for Case 2 using NORIA and the BIEM. The comparison of solutions obtained using NORIA with the exponential representation and the BIEM are in good agreement. The comparison between using the van Genuchten representation in NORIA and the BIEM demonstrates the degree of discrepancy that can result from markedly different permeability functions.

All the NORIA solutions were computed using a uniform mesh consisting of 400 eight-node biquadratic elements. The steady solutions were determined by computing a false transient from an initial pressure field to the final steady state. The initial condition used was a uniform pressure equal to the lower boundary pressure specified on the Dirichlet segment. The BIEM solutions were computed with 16 and 32 boundary elements (4 and 8 nodes per side, respectively), which approximate the variation of the unknown over the element by its value at the midpoint. Results on either mesh were nearly identical. NORIA solutions required about 20 minutes of CPU on the CRAY-XMP to achieve the steady state. The BIEM solutions required about 5 seconds on the VAX 8650.

We emphasize that this does not constitute a study of the relative merits of the finite-element method and the BIEM in terms of run time. That comparison would require a finite-element code developed expressly to solve the linear problem given by (2.17), which would also be much faster. The results computed with NORIA for the exponential conductivity function are based on the nonlinear Richards equation, *i.e.*, the code does not exploit the transformation given by (2.16). Furthermore, the FEM code achieves a steady-state solution by running through a time-consuming false transient. For the nonlinear problem, this guarantees a unique solution for a particular initial condition,

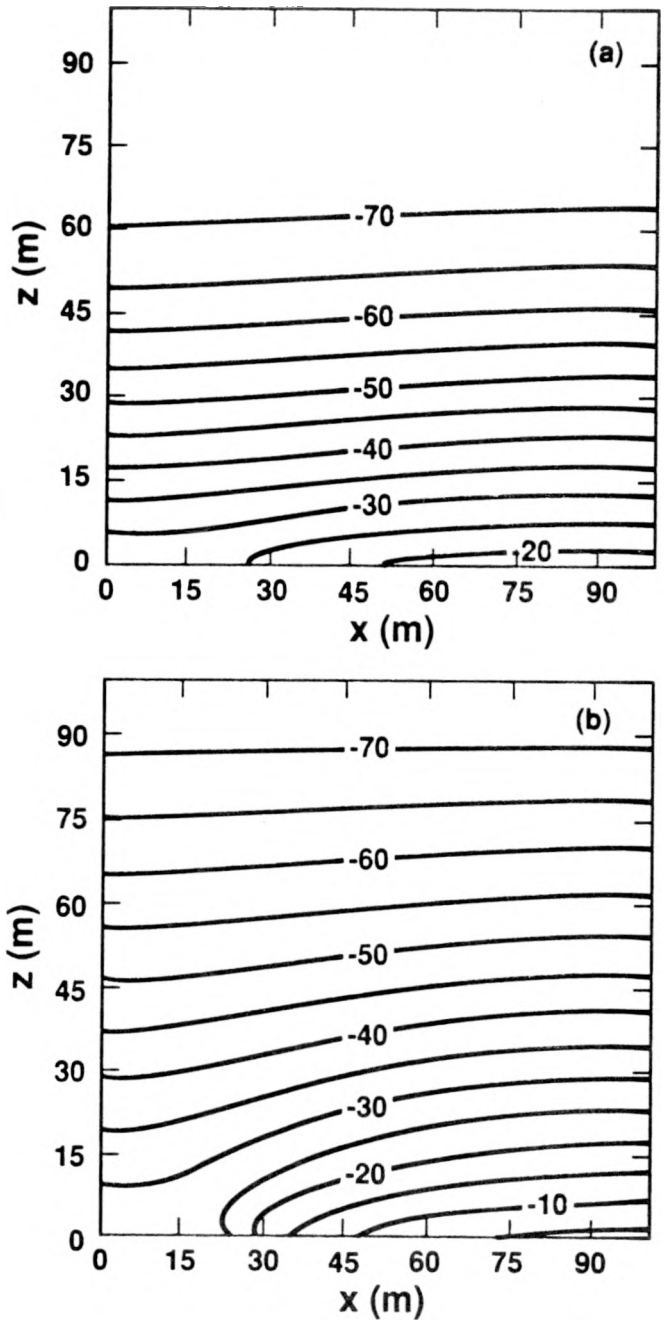

Figure 7.9. Contours of pressure head for Case 2 using (a) the van Genuchten/Mualem permeability model, and (b) the exponential permeability model.

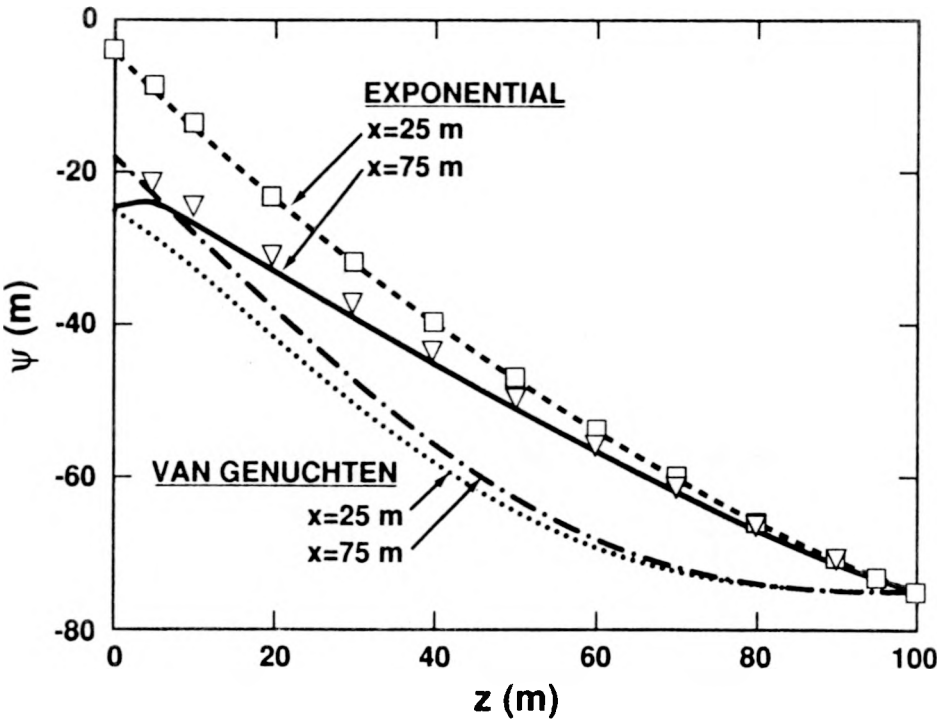

Figure 7.10. Comparison of pressure head profiles along the vertical direction using the van Genuchten and exponential permeability in NORIA (curves) with the BIEM (symbols).

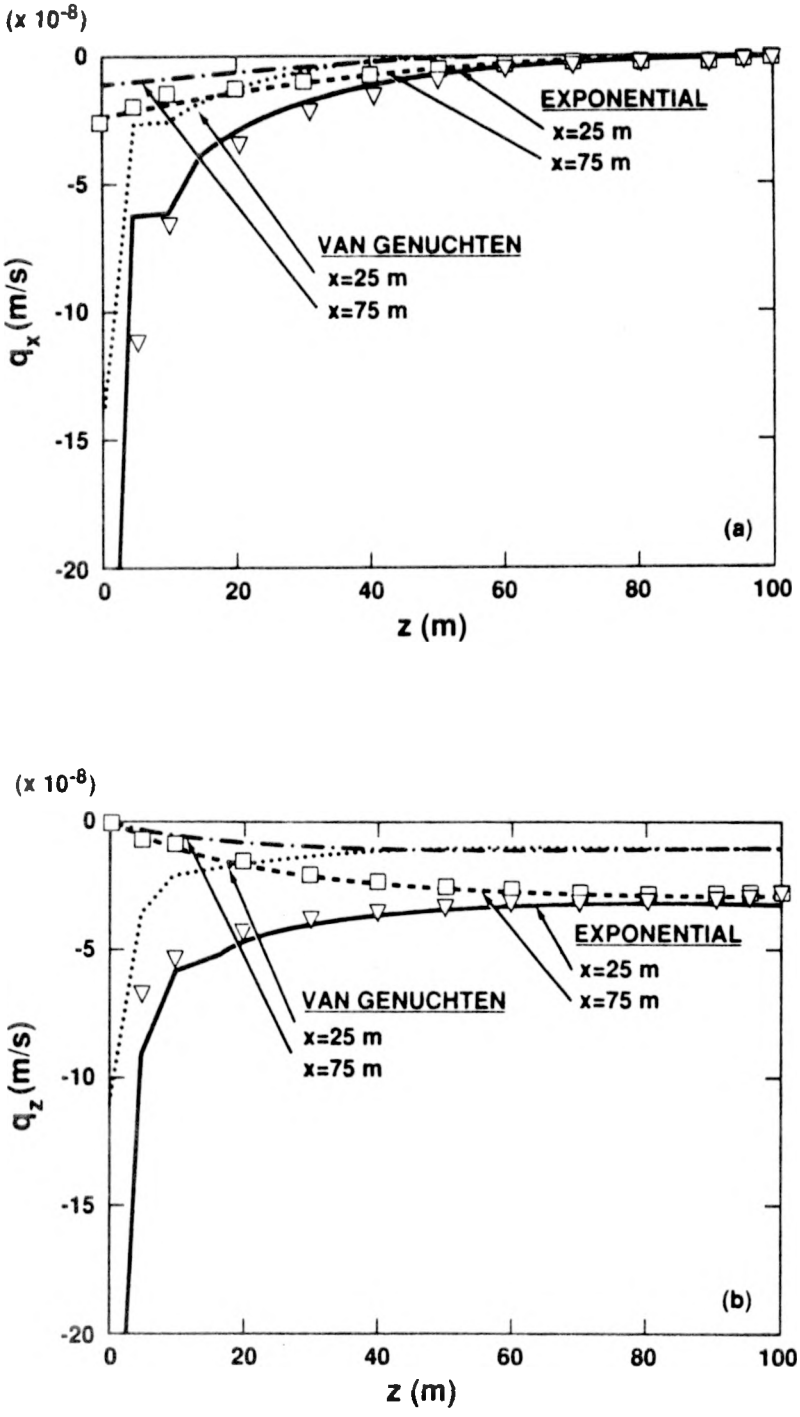

Figure 7.11. Comparison of flux profiles along the vertical direction using the van Genuchten and exponential permeability in NORIA (curves) with the BIEM (symbols); (a) horizontal flux, (b) vertical flux.

but has no advantage for the linear problem. Nonetheless, the comparison of CPU time for the two solution methods is meaningful in terms of *available tools*. That is, should one encounter the need for a steady-state solution under conditions for which the exponential conductivity appears to be a reasonable approximation, the BIEM offers an enormous advantage over currently available alternatives.

8 Summary

The quasi-linear transformation of the steady-state Richards equation assumes that the hydraulic conductivity can be represented by an exponential function of the capillary-pressure head, as was noted many years ago by Gardner (1958). A comparison of the exponential conductivity to the widely used van Genuchten form was carried out for properties believed to be typical of the major tuff units at Yucca Mountain. The exponential has been fit by a simple least-squares method to conductivity "data" generated from the van Genuchten function over the head range from 0 to -150 m. A reasonably good match can be obtained in this fashion for those units that do not exhibit a "shoulder" in the conductivity, *i.e.*, for tuffs that show a relatively small air-entry pressure, including the Tiva Canyon, Topopah Spring, and Calico Hills zeolitic units. In terms of the van Genuchten model parameters, these tuffs are characterized by relatively modest values of β. For tuffs that do exhibit a "shoulder," including the Paintbrush and the Calico Hills vitric units, the exponential model applied in this way yields poor fits. Significant improvement could be obtained by constraining the fit to pressure heads less than that at which the break in slope occurs (for these materials, around -50 m and -25 m, respectively), although we have not pursued this here.

An exact solution for one-dimensional flow based on the exponential model has been compared to numerical solutions based on the van Genuchten model for a representative Yucca Mountain stratigraphy. The agreement is remarkably close at fluxes of 0.1 and 0.5 mm/yr, even in those units for which the exponential conductivity is a poor approximation to the van Genuchten function.

The quasi-linear transformation of the steady-state Richards equation is particularly well suited to solution by the boundary integral equation method, as exploited recently by Pullan and Collins (1987). Indeed, fundamental solutions in both two and three dimensions are well known because of the analog to heat conduction with uniform convection. A BIEM code has been written for plane, two-dimensional domains. The code computes values of potential and/or flux on the domain boundary. The potential and flux can also be computed in the interior, as a postprocessing task, and at any number of arbitrarily placed points. Pathlines and travel times can also be computed if the retention curve for the material is given. The method has shown to exhibit quadratic convergence, even on singular problems, with appropriate mesh grading and has been tested against both analytical and independent numerical solutions with excellent agreement.

9 References

Bixler, N. E., NORIA — A finite element computer program for analyzing water, vapor, and energy transport in porous media, *Sandia National Laboratories Technical Report*, **SAND84–2057**, August 1985. (NNA.870721.0002)

Brebbia, C. A., *The Boundary Element Method for Engineers*, John Wiley and Sons, New York, pp. 1-5, 1978. (NNA.900919.0193)

Brooks, R. H., and A. T. Corey, Properties of porous media affecting fluid flow, *ASCE Journal of the Irrigation and Drainage Division*, **92**, 61–88, 1966. (NNA.870407.0356)

Carslaw, H. S., and J. C. Jaeger, *Conduction of Heat in Solids*, Oxford Press, Oxford, p. 267, 1978. (NNA.900917.0143)

Chandler, G. A., Mesh grading for boundary integral equations, in *Computational Techniques and Applications*, J. Noye and C. Fletcher, eds., Elsevier, New York, 289–296, 1984. (NNA.900919.0171)

Cruse, T. A., Numerical solutions in three-dimensional elastostatics, *International Journal of Solids and Structures*, **5**, 1259-1274, 1969. (NNA.900403.0022)

Gardner, W. R., Some steady-state solutions of the unsaturated moisture flow equation with application to evaporation from a water table, *Soil Science*, **85**, 228-232, 1958. (NNA.900827.0176)

Hills, R. G., ESTIM: A parameter estimation computer program, *Sandia National Laboratories Technical Report*, **SAND87–7063**, August 1987. (NNA.900827.0204)

Hopkins, P. L., COVE 2A Benchmarking Calculations Using LLUVIA, *Sandia National Laboratories Technical Report*, **SAND88–2511**, July, 1990. (NNA.900314.0236)

Hopkins, P. L., and R. R. Eaton, LLUVIA: A program for one-dimensional steady-state flow through partially saturated porous media, *Sandia National Laboratories Technical Report*, **SAND88–0558**, May 1990. (NNA.900406.0001)

Ingham, D. B., and M. A. Kelmanson, Boundary integral equation analyses of singular, potential, and biharmonic problems, in *Lecture Notes in Engineering*, **7**, Springer-Verlag, New York, 1984. (NNA.900522.0258)

Jaswon, M. A., and Symm, G. T., *Integral Methods in Potential Theory and Elastostatics*, Academic Press, New York, 1977. (NNA.900522.0257)

Klavetter, E. A., and R. R. Peters, Estimation of hydrologic properties of an unsaturated fractured rock mass," *Sandia National Laboratories Technical Report*, **SAND84–2642**, July, 1986. (NNA.870317.0738)

Liggett, J. A., and Liu, L-F., *The Boundary Integral Equation Method for Porous Media Flow*, Allen and Unwin, London, pp. 17-33, 1983. (NNA.901130.0016)

Martinez, M. J., and K. S. Udell, Boundary integral analysis of the creeping flow of long bubbles in capillaries, *Journal of Applied Mechanics*, **56**, 211–217, 1989. (NNA.900403.0011)

Mualem, Y., A new model for predicting the hydraulic conductivity of unsaturated porous media, *Water Resources Research*, **12**, 513–522, 1976. (HQS.880517.1803)

Philip, J. R., Steady infiltration from buried point sources and spherical cavities, *Water Resources Research*, **4**, 1039–1047, 1968. (NNA.900131.0230)

Philip, J. R., Theory of infiltration, *Advances in Hydroscience*, **5**, 215-296, 1969. (NNA.900122.0014)

Philip, J. R., Reply to "Comments on steady infiltration from spherical cavities,", *Soil Science Society of America Journal*, **49**, 788–789, 1985. (NNA.900827.0235)

Philip, J. R., The scattering analog for infiltration in porous media, *Reviews of Geophysics*, **27**, 431–448, 1989. (NNA.900711.0066)

Pullan, A. J., The quasilinear approximation for unsaturated porous media flow, *Water Resources Research*, **26**, 1219–1234, 1990. (NNA.901127.0188)

Pullan, A. J., and I. F. Collins, Two- and three-dimensional steady quasi-linear infiltration from buried and surface sources using boundary element techniques, *Water Resources Research*, **23**, 1633–1644, 1987. (NNA.900403.0009)

Rice, J. R., On the degree of convergence of nonlinear spline approximations, in *Approximations with Special Emphasis on Spline Functions, I.*, J. Schoenberg, ed., Academic Press, New York, 1969. (NNA.900917.0136)

Sloan, I. H., and A. Spence, The Galerkin method for integral equations of the first kind with logarithmic kernel: theory and applications, *IMA Journal of Numerical Analysis*, **8**, 105–122, 1988. (NNA.900827.0236)

van Genuchten, M. Th., A closed-form equation for predicting the hydraulic conductivity of unsaturated soils, *Soil Science Society of America Journal*, **44**, 892–898, 1980. (NNA.890522.0287)

Yan, Y., and I. H. Sloan, Mesh grading for integral equations of the first kind with logarithmic kernel, *SIAM Journal of Numerical Analysis*, **26**(3), 574–587, 1989. (NNA.900403.0283)

Appendix A. Calculation of the Flux

We provide here for reference the explicit terms that arise in calculation of the flux. Equation (5.9), in component form, can be written

$$q_x = -\frac{\partial \Phi}{\partial x} \quad , \tag{A.1}$$

$$q_z = -\frac{\partial \Phi}{\partial z} + \alpha \Phi \quad . \tag{A.2}$$

From (5.4), the derivatives of Φ are given by

$$\frac{\partial \Phi}{\partial x}(\mathbf{x}) = -\int_\Gamma \left(\frac{\partial^2 G}{\partial x \partial \chi} n_x + \frac{\partial^2 G}{\partial x \partial \zeta} n_z \right) \Phi d\Gamma + \int_\Gamma \frac{\partial G}{\partial x}(-q_n) d\Gamma \quad , \tag{A.3}$$

$$\frac{\partial \Phi}{\partial z}(\mathbf{x}) = -\int_\Gamma \left(\frac{\partial^2 G}{\partial z \partial \chi} n_x + \frac{\partial^2 G}{\partial z \partial \zeta} n_z \right) \Phi d\Gamma + \int_\Gamma \frac{\partial G}{\partial z}(-q_n) d\Gamma \quad , \tag{A.4}$$

where $\mathbf{x} = (x, z)$ and $\mathbf{y} = (\chi, \zeta)$, and

$$\mathbf{n}(\mathbf{y}) = \begin{pmatrix} n_x \\ n_z \end{pmatrix} (\mathbf{y}) \quad . \tag{A.5}$$

Define

$$\bar{x} = x - \chi \quad ,$$

$$\bar{z} = z - \zeta \quad ,$$

$$r = (\bar{x}^2 + \bar{z}^2)^{1/2} \quad ,$$

$$\varpi = \frac{\alpha}{2} r \quad .$$

The fundamental solution can then be written

$$G(\mathbf{x} \ , \ \mathbf{y}) = \frac{1}{2\pi} \exp\left(\frac{\alpha}{2}\bar{z}\right) K_0(\varpi) \quad , \tag{A.6}$$

and the required derivatives follow in straightforward fashion:

$$\frac{\partial G}{\partial \chi} = -\frac{\partial G}{\partial x} = \frac{\alpha}{4\pi} \frac{\bar{x}}{r} \exp\left(\frac{\alpha}{2}\bar{z}\right) K_1(\varpi) \quad , \tag{A.7}$$

$$\frac{\partial G}{\partial \zeta} = -\frac{\partial G}{\partial z} = \frac{\alpha}{4\pi} \exp\left(\frac{\alpha}{2}\bar{z}\right) \left[\frac{\bar{z}}{r} K_1(\varpi) - K_0(\varpi)\right] \quad , \tag{A.8}$$

$$\frac{\partial^2 G}{\partial x \partial \chi} = \frac{\alpha^2}{8\pi} \exp\left(\frac{\alpha}{2}\bar{z}\right) \left\{ \left[1 - 2\left(\frac{\bar{x}}{r}\right)^2\right] \varpi^{-1} K_1(\varpi) - \left(\frac{\bar{x}}{r}\right)^2 K_0(\varpi) \right\} \quad , \tag{A.9}$$

$$\frac{\partial^2 G}{\partial x \partial \zeta} = \frac{\partial^2 G}{\partial z \partial \chi} = \frac{\alpha^2}{8\pi} \frac{\bar{x}}{r} \exp\left(\frac{\alpha}{2}\bar{z}\right) \left[\left(1 - 2\varpi^{-1}\frac{\bar{z}}{r}\right) K_1(\varpi) - \frac{\bar{z}}{r} K_0(\varpi) \right] \quad , \tag{A.10}$$

$$\frac{\partial^2 G}{\partial z \partial \zeta} = \frac{\alpha^2}{8\pi} \exp\left(\frac{\alpha}{2}\bar{z}\right) \left(\left\{ 2\frac{\bar{z}}{r} + \varpi^{-1} \left[1 - 2\left(\frac{\bar{z}}{r}\right)^2 \right] \right\} K_1(\varpi) - \left[1 + \left(\frac{\bar{z}}{r}\right)^2 \right] K_0(\varpi) \right) \quad . \tag{A.11}$$

The code described here was run on a 32 bit digital machine, representing approximately 7 digits of precision. For this word size, we use the asymptotic approximations to $K_0(\xi)$ and $K_1(\xi)$ for arguments $\xi > 75$ (this value is machine dependent):

$$K_0(\xi) = \sqrt{\frac{\pi}{2\xi}} \exp(-\xi) \left(1 - \frac{1}{8\xi} + \frac{9}{128\xi^2} + \cdots \right) \tag{A.12}$$

$$K_1(\xi) = \sqrt{\frac{\pi}{2\xi}} \exp(-\xi) \left(1 + \frac{3}{8\xi} - \frac{15}{128\xi^2} + \cdots \right) \quad . \tag{A.13}$$

Appendix B. Information from, and Candidate Information for, the Site and Engineering Property Data Base and the Reference Information Base

This report contains no information from the Reference Information Base and contains no candidate information for the Reference Information Base.

This report contains no candidate information for the Site and Engineering Properties Data Base.

DISTRIBUTION LIST

1 John W. Bartlett, Director (RW-1)
Office of Civilian Radioactive
Waste Management
U.S. Department of Energy
Forrestal Bldg.
Washington, D.C. 20585

1 F. G. Peters, Deputy Director (RW-2)
Office of Civilian Radioactive
Waste Management
U.S. Department of Energy
Forrestal Bldg.
Washington, D.C. 20585

1 D. G. Horton (RW-3)
Office of Quality Assurance
Office of Civilian Radioactive
Waste Management
U.S. Department of Energy
Forrestal Bldg.
Washington, D.C. 20585

1 T. H. Isaacs (RW-4)
Office of Strategic Planning
and International Programs
Office of Civilian Radioactive
Waste Management
U.S. Department of Energy
Forrestal Bldg.
Washington, D.C. 20585

1 J. D. Saltzman (RW-5)
Office of External Relations
Office of Civilian Radioactive
Waste Management
U.S. Department of Energy
Forrestal Bldg.
Washington, D.C. 20585

1 Samuel Rousso (RW-10)
Office of Program and Resources
Management
Office of Civilian Radioactive
Waste Management
U.S. Department of Energy
Forrestal Bldg.
Washington, D.C. 20585

1 Carl P. Gertz (RW-20)
Office of Geologic Disposal
Office of Civilian Radioactive
Waste Management
U.S. Department of Energy
Forrestal Bldg.
Washington, D.C. 20585

1 D. E. Shelor (RW-30)
Office of Systems and Compliance
Office of Civilian Radioactive
Waste Management
U.S. Department of Energy
Forrestal Bldg.
Washington, D.C. 20585

1 L. H. Barrett (RW-40)
Office of Storage and Transportation
Office of Civilian Radioactive
Waste Management
U.S. Department of Energy
Forrestal Bldg.
Washington, D.C. 20585

1 F. G. Peters (RW-50)
Office of Contractor Business
Management
Office of Civilian Radioactive
Waste Management
U.S. Department of Energy
Forrestal Bldg.
Washington, D.C. 20585

1 J. C. Bresee (RW-10)
Office of Civilian Radioactive
Waste Management
U.S. Department of Energy
Forrestal Bldg.
Washington, D.C. 20585

1 S. J. Brocoum (RW-20)
Office of Civilian Radioactive
Waste Management
U.S. Department of Energy
Forrestal Building
Washington, D.C. 20585

1 Gerald Parker (RW-30)
Office of Civilian Radioactive
Waste Management
U.S. Department of Energy
Forrestal Bldg.
Washington, D.C. 20585

1 D. U. Deere, Chairman
Nuclear Waste Technical
Review Board
1100 Wilson Blvd. #910
Arlington, VA 22209-2297

5 Carl P. Gertz, Project Manager
Yucca Mountain Project Office
Nevada Operations Office
U.S. Department of Energy
Mail Stop 523
P.O. Box 98518
Las Vegas, NV 89193-8518

1 C. L. West, Director
Office of External Affairs
Nevada Operations Office
U.S. Department of Energy
P.O. Box 98518
Las Vegas, NV 89193-8518

12 Technical Information Office
Nevada Operations Office
U. S. Department of Energy
P.O. Box 98518
Las Vegas, NV 89193-8518

1 P. K. Fitzsimmons, Director
Health Physics & Environmental Division
Nevada Operations Office
U.S. Department of Energy
P.O. Box 98518
Las Vegas, NV 89193-8518

1 Repository Licensing & Quality Assurance Project Directorate
Division of Waste Management
U.S. Nuclear Regulatory Commission
Washington, D.C. 20555

1 Senior Project Manager for Yucca Mountain Repository Project Branch
Division of Waste Management
U.S. Nuclear Regulatory Commission
Washington, D.C. 20555

1 NRC Document Control Desk
Division of Waste Management
U.S. Nuclear Regulatory Commission
Washington, D.C. 20555

1 E. P. Binnall
Field Systems Group Leader
Building 50B/4235
Lawrence Berkeley Laboratory
Berkeley, CA 94720

1 Center for Nuclear Waste Regulatory Analyses
6220 Culebra Road
Drawer 28510
San Antonio, TX 78284

3 L. J. Jardine
Technical Project Officer for YMP
Lawrence Livermore National Laboratory
Mail Stop L-204
P.O. Box 808
Livermore, CA 94550

4 R. J. Herbst
Technical Project Officer for YMP
Los Alamos National Laboratory
N-5, Mail Stop J521
P.O. Box 1663
Los Alamos, NM 87545

1 H. N. Kalia
Exploratory Shaft Test Manager
Los Alamos National Laboratory
Mail Stop 527
101 Convention Center Dr.
Suite 820
Las Vegas, NV 89109

1 J. F. Divine
Assistant Director for Engineering Geology
U.S. Geological Survey
106 National Center
12201 Sunrise Valley Dr.
Reston, VA 22092

6 L. R. Hayes
Technical Project Officer for YMP
U.S. Geological Survey
P.O. Box 25046
421 Federal Center
Denver, CO 80225

1 D. Zesiger
U.S. Geological Survey
101 Convention Center Dr.
Suite 860 - MS509
Las Vegas, NV 89109

1 DeWayne A. Campbell
YMP Technical Project Officer
Bureau of Reclamation
P.O. Box 25007 Bldg. 67
Denver, CO 80225-0007

1 K. W. Causseaux
NHP Reports Chief
U.S. Geological Survey
P.O. Box 25046
421 Federal Center
Denver, CO 80225

1 R. V. Watkins, Chief
Project Planning and Management
U.S. Geological Survey
P.O. Box 25046
421 Federal Center
Denver, CO 80225

1 V. M. Glanzman
U.S. Geological Survey
P.O. Box 25046
913 Federal Center
Denver, CO 80225

1 J. H. Nelson
Technical Project Officer for YMP
Science Applications International Corp.
101 Convention Center Dr.
Suite 407
Las Vegas, NV 89109

2 SAIC-T&MSS Library
Science Applications International Corp.
101 Convention Center Dr.
Suite 407
Las Vegas, NV 89109

1 Elaine Ezra
YMP GIS Project Manager
EG&G Energy Measurements, Inc.
Mail Stop D-12
P.O. Box 1912
Las Vegas, NV 89125

1 W. M. Hewitt, Program Manager
Roy F. Weston, Inc.
955 L'Enfant Plaza, Southwest
Suite 800
Washington, D.C. 20024

1 Technical Information Center
Roy F. Weston, Inc.
955 L'Enfant Plaza, Southwest
Suite 800
Washington, D.C. 20024

1 D. L. Fraser, General Manager
Reynolds Electrical & Engineering Co.
P.O. Box 98521
Mail Stop 555
Las Vegas, NV 89193-8521

1 Robert F. Pritchett
Technical Project Officer for YMP
Reynolds Electrical & Engineering Co.
Mail Stop 615
P.O. Box 98521
Las Vegas, NV 89193-8521

1 A. E. Gurrola
General Manager
Raytheon, Inc.
Mail Stop 580
P.O. Box 93838
Las Vegas, NV 89193-3838

1 James C. Calovini
Raytheon Services, Inc.
101 Convention Center Dr.
Suite P-280
Las Vegas, NV 89109

1 D. L. Lockwood, General Manager
Raytheon Services, Inc.
Mail Stop 514
P.O. Box 93265
Las Vegas, NV 89193-3265

1 Richard L. Bullock
Technical Project Officer for YMP
Raytheon Services, Inc.
101 Convention Center Dr.
Suite P250
Las Vegas, NV 89109

1 R. E. Lowder
Technical Project Officer for YMP
MAC Technical Services
Valley Bank Center
101 Convention Center Drive
Suite 1100
Las Vegas, NV 89109

1 D. J. Bales
Science and Technology Division
Office of Scientific and Technical Information
U.S. Department of Energy
P.O. Box 62
Oak Ridge, TN 37831

1 Carlos G. Bell, Jr.
Professor of Civil Engineering
Civil and Mechanical Engineering Department
University of Nevada, Las Vegas
4505 South Maryland Parkway
Las Vegas, NV 89154

1 C. F. Costa, Director
Nuclear Radiation Assessment Division
U.S. Environmental Protection Agency
Environmental Monitoring Systems Laboratory
P.O. Box 93478
Las Vegas, NV 89193-3478

1 ONWI Library
Battelle Columbus Laboratory
Office of Nuclear Waste Isolation
505 King Avenue
Columbus, OH 43201

1 T. Hay, Executive Assistant
Office of the Governor
State of Nevada
Capitol Complex
Carson City, NV 89710

3 R. R. Loux, Jr.
Executive Director
Nuclear Waste Project Office
State of Nevada
Evergreen Center, Suite 252
1802 North Carson Street
Carson City, NV 89710

1 C. H. Johnson
Technical Program Manager
Nuclear Waste Project Office
State of Nevada
Evergreen Center, Suite 252
1802 North Carson Street
Carson City, NV 89710

1 John Fordham
Water Resources Center
Desert Research Institute
P.O. Box 60220
Reno, NV 89506

1 Dr. Martin Mifflin
Desert Research Institute
Water Resources Center
2505 Chandler Avenue
Suite 1
Las Vegas, NV 89120

1 Eric Anderson
Mountain West Research-Southwest Inc.
2901 N. Central Ave. #1000
Phoenix, AZ 85012-2730

1 Department of Comprehensive Planning
Clark County
225 Bridger Avenue, 7th Floor
Las Vegas, NV 89155

1 Planning Department
Nye County
P.O. Box 153
Tonopah, NV 89049

1 Lincoln County Commission
Lincoln County
P.O. Box 90
Pioche, NV 89043

5 Judy Foremaster
City of Caliente
P.O. Box 158
Caliente, NV 89008

1 Economic Development Department
City of Las Vegas
400 East Stewart Avenue
Las Vegas, NV 89109

1 Community Planning & Development
City of North Las Vegas
P.O. Box 4086
North Las Vegas, NV 89030

1 Director of Community Planning
City of Boulder City
P.O. Box 367
Boulder City, NV 89005

1 Commission of the European
Communities
200 Rue de la Loi
B-1049 Brussels
Belgium

1	6300	T. O. Hunter, Actg.
1	6310	T. E. Blejwas, Actg.
1	6310A	L. E. Shephard
1	6311	A. L. Stevens
1	6312	F. W. Bingham
1	6312	G. E. Barr
1	6312	P. G. Kaplan
1	6312	F. C. Lauffer
1	6312	R. W. Barnard
1	6313	L. S. Costin
1	6313	M. E. Fewell
1	6313	A. H. Treadway
1	6315	F. B. Nimick, Actg.
1	6316	R. P. Sandoval
1	6317	S. Sinnock
2	6318	L. J. Erickson for 100/12149/SAND90-0253/NQ
1	6318	R. J. Macer for Accession No. Data Base
1	6319	R. R. Richards
1	6416	J. T. McCord
1	1510	J. C. Cummings
1	1511	J. S. Rottler
1	1511	R. R. Eaton
1	1511	P. L. Hopkins
15	1511	M. J. Martinez
15	1511	D. F. McTigue
1	1512	A. C. Ratzel
1	1513	R. D. Skocypec
1	1513	R. C. Dykhuizen
1	1520	L. W. Davison
1	1530	J. R. Asay
1	1550	C. W. Peterson
5	3141	S. A. Landenberger
8	3145	Document Processing for DOE/OSTI
3	3151	G. C. Claycomb
1	3223	P. A. Davis
20	6341	WMT Library
1	6410	D. J. McCloskey, Actg.
1	8523	Technical Library

The number in the lower right-hand corner is an accession number used for Office of Civilian Radioactive Waste Management purposes only. It should not be used when ordering this publication.

Org.	Bldg.	Name	Rec'd by	Org.	Bldg.	Name	Rec'd by

Sandia National Laboratories